CONVECTION-REACTION EQUATION BASED MAGNETIC RESONANCE ELECTRICAL PROPERTIES TOMOGRAPHY (CR-MREPT)

A THESIS

SUBMITTED TO THE DEPARTMENT OF ELECTRICAL AND

ELECTRONICS ENGINEERING

AND THE GRADUATE SCHOOL OF ENGINEERING AND SCIENCE

OF BILKENT UNIVERSITY

IN PARTIAL FULFILLMENT OF THE REQUIREMENTS

FOR THE DEGREE OF

MASTER OF SCIENCE

By

Fatih Süleyman Hafalır

August, 2013

I certify that I have read this thesis and that in my opinion it is fully adequate, in scope and in quality, as a thesis for the degree of Master of Science.

Prof. Dr. Yusuf Ziya İder(Advisor)

I certify that I have read this thesis and that in my opinion it is fully adequate, in scope and in quality, as a thesis for the degree of Master of Science.

Assoc. Prof. Dr. Vakur B. Ertürk

I certify that I have read this thesis and that in my opinion it is fully adequate, in scope and in quality, as a thesis for the degree of Master of Science.

Prof. Dr. Nevzat Güneri Gençer

Approved for the Graduate School of Engineering and Science:

Prof. Dr. Levent Onural
Director of the Graduate School

ABSTRACT

CONVECTION-REACTION EQUATION BASED MAGNETIC RESONANCE ELECTRICAL PROPERTIES TOMOGRAPHY (CR-MREPT)

Fatih Süleyman Hafalır
M.S. in Electrical and Electronics Engineering
Supervisor: Prof. Dr. Yusuf Ziya İder
August, 2013

Tomographic imaging of electrical conductivity and permittivity of tissues may be used for diagnostic purposes as well as for estimating local specific absorption rate (SAR) distributions. Magnetic Resonance Electrical Properties Tomography (MREPT) aims at noninvasively obtaining conductivity and permittivity images at RF frequencies of MRI systems. MREPT algorithms are based on measuring the B_1 field which is perturbed by the electrical properties of the imaged object. In this study, the relation between the electrical properties and the measured B_1^+ field is formulated, for the first time as, the well-known convection-reaction equation. The suggested novel algorithm, called "cr-MREPT", is based on the solution of this equation, and in contrast to previously proposed algorithms, it is applicable in practice not only for regions where electrical properties are relatively constant but also for regions where they vary. The convection-reaction equation is solved using a triangular mesh based finite difference method and also finite element method (FEM).

The convective field of the convection-reaction equation depends on the spatial derivatives of the B_1^+ field. In the regions where the magnitude of convective field is low, a spot-like artifact is observed in the reconstructed conductivity and dielectric permittivity images. For eliminating this artifact, two different methods are developed, namely "constrained cr-MREPT" and "double-excitation cr-MREPT". In the constrained cr-MREPT method, in the region where the magnitude of convective field is low, the electrical properties are reconstructed by neglecting the convective term in the equation. The obtained solution is used as a constraint for solving electrical properties in the whole domain. In the double-excitation cr-MREPT method, two B_1 excitations, which create two convective field distributions having low magnitude of convective field in different

locations, are applied separately. The electrical properties are then reconstructed simultaneously using data from these two applied B_1^+ field.

These methods are tested with both simulation and experimental data from phantoms. As seen from results, successful electrical property reconstructions are obtained in all regions including electrical property transition region. The performance of cr-MREPT method against noise is also investigated.

Keywords: B_1 mapping, conductivity imaging, convection-reaction equation, Magnetic Resonance Electrical Properties Tomography, MREPT, MREIT, permittivity imaging, quantitative MRI, triangular mesh, FEM.

ÖZET

TAŞIMA-REAKSİYON DENKLEMİ TEMELLİ MANYETİK REZONANS ELEKTRİKSEL ÖZELLİKLER TOMOGRAFİSİ (TR-MREÖT)

Fatih Süleyman Hafalır
Elektrik ve Elektronik Mühendisliği, Yüksek Lisans
Tez Yöneticisi: Prof. Dr. Yusuf Ziya İder
Ağustos, 2013

Dokuların elektrik iletkenliğinin ve dielektirik geçirgenliğinin tomografik görüntülenmesi teşhis amaçıyla kullanılabildiği gibi lokal özgül soğurma oranı (SAR) dağılımlarını kestirmek için de kullanılabilmektedir. Manyetik Rezonans Elektriksel Özellikler Tomografisi (MREÖT), MRG sistemlerinin RF frekansında elektriksel iletkenlik ve dielektrik geçirgenlik görüntülerinin noninvaziv olarak elde edilmesini amaçlamaktadır. MREÖT algoritmaları, görüntülenen cismin elektriksel özellikleri tarafından bozulan B_1 manyetik alanın ölçülmesine dayanmaktadır. Bu çalışmada, elektriksel özellikler ile ölçülen B_1^+ manyetik alanı arasındaki ilişki bilinen taşınım-reaksiyon denklemi olarak ilk defa formüle edilmiştir. Önerilen bu yeni algoritma "tr-MREÖT" olarak adlandırılmış ve bu denklemin çözümüne dayanmaktadır. Önceki önerilen algoritmaların tersine, sadece elektriksel özelliklerin göreceli olarak sabit olduğu bölgelerde değil aynı zamanda değiştiği bölgelerde de bu algoritma pratikte uygulanabilir. Taşınım-reaksiyon denklemi, üçgen örgülere dayalı sonlu farklar yöntemi ve sonlu eleman yöntemi (FEM) kullanılarak çözüldü.

Taşınım-reaksiyon denklemindeki konveksiyon alanı, B_1^+ manyetik alanın uzaysal türevlerine bağlıdır. Konveksiyon alanın genliğinin düşük olduğu bölgelerde, geriçatılmış elektriksel iletkenlik ve dielektrik geçirgenlik görüntülerinde benek gibi hatalar gözlemlenmektedir. Bu hataları gidermek için, "kısıtlı tr-MREÖT" ve "çift-uyarma tr-MREÖT" adlandırılan iki farklı yöntem geliştirildi. Kısıtlı tr-MREÖT yönteminde, konveksiyon alanının genliğinin düşük olduğu bölgelerde, denklemin konveksiyon terimi ihmal edilerek elektriksel özellikler geriçatıldı. Elde edilen çözüm, tüm bölgede elektriksel özelliklerini çözmek için kısıt olarak kullanıldı. Çift-uyarma tr-MREÖT yönteminde, farklı bölgelerde genliği düşük konveksiyon alanına sahip iki B_1 manyetik alanı ayrı ayrı uygulandı. Daha sonra

elektriksel özellikler, uygulanan bu B_1^+ manyetik alan verileri eş zamanlı kullanılarak geriçatıldı.

Bu yöntemler, fantomlar kullanılarak yapılan simülasyon ve deney verileri kullanılarak test edildi. Sonuçlardan görüldüğü gibi başarılı elektriksel özellik geriçatılmaları, elektriksel özelliklerin değişim bölgelerini de içerecek şekilde bütün bölgelerde elde edildi. Tr-MREÖT yönteminin gürültüye karşı performansı da incelendi.

Anahtar sözcükler: B_1 haritalama, elektriksel iletkenlik görüntüleme, taşınım-reaksiyon denklemi, Manyetik Rezonans Elektriksel Özellikler Tomografisi, MREÖT, MREET, dielektrik geçirgenlik görüntüleme, niceliksel MRG, üçgen örgü, sonlu eleman yöntemi.

Acknowledgement

First of all, I am greatly indebted to my supervisor Prof. Dr. Yusuf Ziya İder for his support, encouragement, patience and instructive comments throughout my graduate study.

I would like to express my special thanks and gratitude to Assoc. Prof. Dr. Vakur B. Ertürk and to Prof. Dr. Nevzat Güneri Gençer the members of my jury, for showing their keen interest to the subject matter, reading and commenting on the thesis.

I would also like to thank the The Scientific and Technological Research Council of Turkey (TUBITAK) for providing financial support during my graduate study.

I wish to extend my special thanks to my office mates Ömer Faruk Oran, Necip Gürler and Mustafa Rıdvan Cantaş for their valuable help and support. I especially would like to thank my friends Ali Alp Akyol, Furkan Çimen, Furkan Keskin, Ali Cahit Köşger, Serkan Sarıtaş, Fatih Emre Şimşek, Taha Ufuk Taşcı, Uğur Yılmaz and Ahmet Yükseltürk who have been on my side during my happy and difficult days in these last three years. I would like to express my gratitude to my dear friends in Bilkent Orienteering Club.

I wish to express my deep gratitude to my parents and brothers Tarık and Abdullah, for their support, patience and sincere love. There are no words to express my gratitude to my girlfriend Nilgün Öz for her unconditional love, support, patience and encouragement. She has always been there for me through my ups and downs.

Contents

List of Figures

List of Tables

Chapter 1

Introduction

1.1 Motivation

Tomographic imaging of electrical properties of biological tissues has been the subject of research for decades since it is useful for monitoring and diagnostic purposes [1]-[7]. Ex vivo studies on brain tissue in connection with stroke show significant changes of conductivity and permittivity [8]. Also, the studies reported that tumors can be characterized by their electrical properties, identifying between healthy and malignant tissue [3]. On the other hand, it is known that electrical properties of tissues depend on frequency and electrical properties at RF frequencies are important parameters in the field of RF safety. The electrical conductivity at RF frequencies is needed to correctly estimate the local specific energy absorption rate (SAR), which is directly related to tissue heating. The local heating of tissue is a major problem in high-field magnetic resonance (MR), particularly in the framework of parallel transmission [9].

In the past two decades, there have been many studies on imaging of electrical properties. Well-known methods of imaging electrical properties in vivo are electrical impedance tomography (EIT) and its variants using magnetic induction tomography (MIT). They are developed to image electrical conductivity (σ) and dielectric permittivity (ε) of tissues in the frequency range 1 kHz to 1

MHz [10]-[15]. In these methods, current is either injected into the body by surface electrodes (EIT), or induced in the body using external coils (MIT), and data is measured either on the surface of the body or outside the body. Consequently, low spatial resolution is achieved especially for interior regions of the body because measured data are less sensitive to the variations of the electrical properties of such regions. In order to improve spatial resolution in the relatively interior regions, Magnetic Resonance Electrical Impedance Tomography (MREIT) has been proposed [16]-[22]. In MREIT, internal magnetic field generated by the internal current distribution is imaged with high resolution using magnetic resonance imaging (MRI) techniques [23], [24]. Thereby local magnetic field perturbations due to local conductivity perturbations are sensitively measured resulting in higher spatial resolution throughout the inside. Currently MREIT is suitable for DC or below 1 kHz imaging of conductivity.

Besides the above mentioned techniques, several electrical property imaging techniques have been developed for the RF frequencies used in high field MR systems such as 1.5 T or higher and these are in general named Magnetic Resonance Electric Properties Tomography (MREPT) [25]-[28]. These techniques exploit the fact that the electrical properties of the imaged object perturb the RF magnetic field of the MRI system. Therefore, the MREPT methods are based on a measurement of the complex RF magnetic field of the MRI system. The electrical properties of the object are reconstructed using these measurements. In principle, MREPT is able to reconstruct not only the electrical conductivity but also the permittivity.

1.2 Review of Previous Studies in MREPT

The possibility to extract electrical properties directly from MRI images was addressed by Haacke *et al.* [29]. They stated that when the electrical properties are increased, the more the RF profile is disrupted in MRI. Then, they suggested that the electrical properties can be estimated using MRI images that reflect the disrupted RF profile and they proposed a method to extract electrical properties

by using iterative sensitivity matrix algorithm. Moreover, these authors used heterogeneous planar model to evaluate the effects of object size, object geometry and signal to noise ratio (SNR) in extracting the conductivity and permittivity.

Wen has developed a modified Helmholtz equation based non-iterative algorithm [25] whereby the conductivity and permittivity are estimated by

$$\sigma = -\frac{\mathrm{Im}(\nabla^2 B_1^+ / B_1^+)}{\mu_0 \omega} \quad \text{and} \quad \varepsilon = -\frac{\mathrm{Re}(\nabla^2 B_1^+ / B_1^+)}{\mu_0 \omega^2} \tag{1.1}$$

where B_1^+ is the MR-wise active circularly polarized (left-handed rotating) component of the RF field. In this method, B_1^+ magnitude map is found using the well-known double-angle B_1 mapping technique [30] and B_1^+ phase distribution is assumed to be half of the spin-echo MR phase image. Then, the author tested the algorithm with phantom and animal experiments using 1.5 and 4.7 T MRI.

Katscher *et al.* proposed an iterative algorithm derived from Ampere's Law to image the electrical properties and they conducted an *in vivo* experiments on a human head and leg using a 3 T MRI system [31]. Later, Katscher *et al.* proposed an algorithm similar to Wen's but which is more robust to noise [26]. In this method, assuming that the electrical properties are constant within an integration area A, the authors proposed the following reconstruction formula:

$$\kappa(\mathbf{r}) = \varepsilon(\mathbf{r}) - i\sigma(\mathbf{r})/\omega = \frac{\oint_{\partial A} \nabla \times \mathbf{H}(\mathbf{r}) \cdot \mathrm{d}\mathbf{l}}{\mu\omega^2 \int_A \mathbf{H}(\mathbf{r}) \cdot \mathrm{d}\mathbf{a}} \tag{1.2}$$

where ∂A is the boundary of A, $\mathrm{d}\mathbf{l}$ is the line element, and $\mathrm{d}\mathbf{a}$ is the surface element. The formula (1.2) is an implementation of a local average of Wen's equation (1.1), and it does not require the explicit calculation of the second spatial derivatives of the magnetic field components. They suggested that the H_x and H_y components can be determined by positive and negative rotating magnetic field components (H^+ and H^-). In this study, H^+ magnitude map is determined by actual flip angle imaging (AFI) [32] and same as Wen's method, H^- phase distribution is assumed to be half of the spin-echo MR phase image. In order to determine H^- and H_z, the authors suggested that H^- and H_z can be derived from a full model of the RF coil with or without the patient, or assumed $H^- \equiv 0$ and/or $H_z \equiv 0$ due to $H^+ \gg H^-$, H_z for a birdcage coil (note that z-direction is

taken as the direction of the DC magnetic field of an MRI system). Both Wen's, and Katscher *et al.*'s algorithms are suitable for reconstructing conductivity and permittivity in regions where these properties are almost constant.

Zhang *et al.* have developed a dual-excitation algorithm [27] whereby the complex permittivity ($\varepsilon_c = \varepsilon_r\varepsilon_0 - i\sigma/\omega$) is reconstructed based on the equations:

$$\begin{aligned} -\nabla^2 H_x &= \omega^2\mu_0 H_x\varepsilon_c - \tfrac{1}{\varepsilon_c}\tfrac{\partial H_x}{\partial z}\tfrac{\partial \varepsilon_c}{\partial z} + \tfrac{1}{\varepsilon_c}\left(\tfrac{\partial H_y}{\partial x} - \tfrac{\partial H_x}{\partial y}\right)\tfrac{\partial \varepsilon_c}{\partial y} \\ -\nabla^2 H_x &= \omega^2\mu_0 H_y\varepsilon_c - \tfrac{1}{\varepsilon_c}\tfrac{\partial H_y}{\partial z}\tfrac{\partial \varepsilon_c}{\partial z} + \tfrac{1}{\varepsilon_c}\left(\tfrac{\partial H_y}{\partial x} - \tfrac{\partial H_x}{\partial y}\right)\tfrac{\partial \varepsilon_c}{\partial x} \end{aligned} \tag{1.3}$$

These equations (1.3) are derived from Maxwell's equations and H_z components of applied RF magnetic field are assumed to be negligible for birdcage and transverse electromagnetic (TEM) coils. Using data which are collected for two different linear RF excitations, a total of four equations are derived in which complex permittivity (ε_c), and its 3 spatial derivatives appear as the unknown variables. By solving these equations, conductivity and permittivity are reconstructed. In this study, the algorithm is tested by using simulations of human brain. These investigators assume that the H_x and H_y components of the excitation RF field can be measured, and therefore this method is not easily applicable to most clinical MRI scanners at present.

In Voigt *et al.*'s method [33], the conductivity distributions can be reconstructed from phase images and permittivity distributions can be reconstructed from magnitude images of the RF transmit field, approximately. Starting from Katscher *et al.*'s formula (1.2), the conductivity and permittivity values are approximated as

$$\sigma \approx \frac{1}{\mu_0\omega V}\oint_{\partial V}\nabla\varphi_+(\mathbf{r})\cdot d\mathbf{a} \quad \text{and} \quad \varepsilon \approx \frac{\oint_{\partial V}\nabla\left|B_1^+(\mathbf{r})\right|\cdot d\mathbf{a}}{\mu_0\omega^2\int_V\left|B_1^+(\mathbf{r})\right|dV} \tag{1.4}$$

where φ_+ is the phase of B_1^+, V is the integration volume, ∂V is the surface of V, and $d\mathbf{a}$ is the surface element. The feasibility studies of this phase-based conductivity imaging and magnitude-based permittivity imaging are done by numerical simulations and *in vivo* experiments on human brain.

Later, van Lier *et al.* suggested B_1^+ phase can be derived directly from the measurable transceive phase, $arg(B_1^+B_1^-)$, in the head. Measured phase (φ_s)

depends on the transceive phase ($\varphi_{\pm}$), the off-resonant terms and the eddy current induced magnetic field (B_e):

$$\varphi_S(\mathbf{r}, T_E) = \varphi_{\pm}(\mathbf{r}) - \omega_{off-res}(\mathbf{r})\, T_E + \int_0^{T_E} \gamma B_e dt \tag{1.5}$$

where T_E is echo-time. These authors assumed that the transmit phase (φ_+) is half of the transceive phase ($\varphi_{\pm}$). This assumption is valid for some situations for example for a dielectrically homogeneous lossy cylinder using quadrature excitation and reception with the same coil. Then, using only B_1^+ phase, the conductivity is reconstructed approximately as

$$\sigma \approx -\mathrm{Im}\left(\frac{\nabla^2 e^{i\varphi_+}}{e^{i\varphi_+}}\right)\frac{1}{\mu_0\omega} \tag{1.6}$$

where φ_+ is the phase of B_1^+. In this study, this method is tested for a human head excited by 7T birdcage coil using simulation and measurements. The algorithms proposed by van Lier *et al.* and Voigt *et al.* are also suitable for regions where the electrical properties are almost constant.

Seo *et al.* pointed out the current MREPT methods rely on an assumption of a locally homogeneous electrical properties and a reconstruction error occurs where this assumption fails [34]. They analyzed the reconstruction error quantitatively by performing numerical simulations and phantom experiments.

Recently, Sodickson *et al.* proposed a method called Local Maxwell Tomography (LMT) which is free of assumption on RF phase [35]. Using complementary information from the transmit and receive sensitivity distributions of multiple coils, this method solves RF phase distribution along with unknown electrical properties. In this method, the transmit and receive fields are expressed as:

$$B_{1,l}^+ = \left(\left|B_{1,l}^+\right| e^{i\varphi_{\Sigma_l}}\right)\left(e^{-i\varphi_0}\right) \text{ and } \; B_{1,l'}^- = \left(\left|MB_{1,l'}^-\right| e^{i\varphi_{\Delta_{l'}}}\right)\left(|M|^{-1} e^{i\varphi_0}\right) \tag{1.7}$$

where φ_0 is the unknown phase distribution associated with a chosen reference receive coil and $|M|$ is the unknown magnetization. l labels transmit, and l' receive coils. φ_{Σ_l} is the sum of transmit and reference phase, $\varphi_{\Delta_l'}$ is the difference of receive and reference phase. Using product rule expansion of $\nabla^2 B_1^{\pm}$, separation into real and imaginary parts, and assuming electrical properties are locally

homogeneous, the Helmholtz equation is written in terms of receive and transmit fields in matrix equations as follow (constant M):

$$\begin{bmatrix} -2\partial \ln\left|B_{1,l}^{+}\right|/\partial x & -2\partial \ln\left|B_{1,l}^{+}\right|/\partial y & -2\partial \ln\left|B_{1,l}^{+}\right|/\partial z & -1 & 1 \\ 2\partial \ln\left|MB_{1,l'}^{-}\right|/\partial x & 2\partial \ln\left|MB_{1,l'}^{-}\right|/\partial y & 2\partial \ln\left|MB_{1,l'}^{-}\right|/\partial z & 1 & 1 \end{bmatrix}.$$
$$\begin{bmatrix} \frac{\partial\varphi_0}{\partial x} & \frac{\partial\varphi_0}{\partial y} & \frac{\partial\varphi_0}{\partial z} & \nabla^2\varphi_0 & \omega\mu\sigma \end{bmatrix}^T = \begin{bmatrix} -2\nabla \ln\left|B_{1,l}^{+}\right| \cdot \nabla\varphi_{\Sigma_l} - \nabla^2\varphi_{\Sigma_l} \\ -2\nabla \left|MB_{1,l'}^{-}\right| \cdot \nabla\varphi_{\Delta_{l'}} - \nabla^2\varphi_{\Delta_{l'}} \end{bmatrix} \tag{1.8}$$

Similar equation can also be written for dielectric permittivity. Since there are 5 unknowns, a 3-element transmit-receive array will suffice to determine conductivity and dielectric permittivity and larger numbers of elements will improve robustness. In this study, the algorithm is tested by using simulations and experiments of phantoms. This algorithm enables electrical property mapping without assumptions regarding phase and field structure. However, it is also suitable for regions that have homogeneous electrical properties.

1.3 Objective and Scope of the Thesis

Imaging of electrical properties (EP) of tissues (conductivity σ and permittivity ε) using MRI is important to provide diagnostic information about tissues and patient-specific real-time SAR calculation. Magnetic Resonance Electrical Properties Tomography (MREPT) achieves non-invasive electrical property mapping using the measured complex B1 field at Larmor frequency. Currently available practical MREPT methods reconstruct electrical properties within local homogeneous regions where conductivity and dielectric permittivity values are almost constant. In this thesis, we propose a novel algorithm named convection-reaction equation based MREPT (cr-MREPT) which reconstructs conductivity and dielectric permittivity also in transition regions where conductivity and dielectric permittivity vary.

This thesis is confined to the reconstruction of tissue conductivity and dielectric permittivity or equivalently admittivity defined as $\gamma = \sigma + i\omega\varepsilon$, where ω is the frequency of the applied RF field. Imaging of magnetic permeability

is not considered, and it is assumed that tissues have the free space magnetic permeability.

Starting from the Maxwell's equations, we derive a partial differential equation for admittivity, γ, which is in the form of the convection-reaction equation where the coefficients of the equation depend on the complex B_1^+ map. The derived equation is then solved using a triangular mesh based finite difference method and finite element method (FEM) to reconstruct conductivity and permittivity for single or double RF excitation cases. The convective field of the convection-reaction equation depends on the spatial derivatives of the B_1^+ field, and in the regions where its magnitude is low, a spot-like artifact is observed in the reconstructed electrical properties images. For eliminating this artifact, two different methods are developed, namely "constrained cr-MREPT" and "double-excitation cr-MREPT". The proposed method is suitable for reconstructing electrical properties not only in regions where they are relatively constant but also in regions where they change. Reconstructions are made using noise-free and noisy simulated data and also from experimental data.

1.4 Organization of the Thesis

The thesis is organized as follows: Chapter 2 describes the derivation of the proposed convection-reaction equation based MREPT (cr-MREPT) algorithm. In Chapter 3, a triangular mesh based finite difference method is explained for solution of the convection-reaction equation based MREPT (cr-MREPT) algorithm. Then, the simulation methods include birdcage coil modeling and also the description of simulation phantoms. The preparation of the experimental phantom, the experiment procedures and the measuring method of complex B_1^+ mapping are also explained in this chapter. In Chapter 4, the simulation and experimental results are given. In the preliminary results, the spot-like artifacts are observed. For eliminating these artifacts, two different methods namely "constrained cr-MREPT" and "double-excitation cr-MREPT" are suggested in this chapter. In addition, the noise behavior of the cr-MREPT algorithm is also analyzed. In

Chapter 5, the cr-MREPT algorithm using finite element method (FEM) is described and also using this method, the simulation and experimental studies are given. Chapter 6 includes discussion of the proposed cr-MREPT algorithm and concludes the thesis.

Chapter 2

Theory

Let $\mathbf{H}$ represent the RF magnetic field generated by the RF coil at Larmor frequency inside the object to be imaged. $\mathbf{H}$ is determined by the geometry of the coil and is also influenced by the presence (loading effect) of the object. The loading effect of the object is related to its electrical properties, and specifically to its admittivity which is defined as $\gamma = \sigma + i\omega\varepsilon$ where σ is electrical conductivity and ε is dielectric permittivity. Although the influence of γ on $\mathbf{H}$ is not desired in conventional imaging because it destroys the homogeneity of the RF field within the object, in MREPT, this influence is exploited. The purpose of this section is therefore to relate the perturbation in $\mathbf{H}$ to the admittivity distribution of the object, so that if $\mathbf{H}$ can be measured then an inverse problem may be solved to find admittivity.

Components of $\mathbf{H}$ can be expressed in terms of the left-handed rotating and right-handed rotating RF fields H^+, and H^- respectively defined as $H^+ = (H_x + iH_y)/2$, and $H^- = (H_x - iH_y)^*/2$ such that $\mathbf{H} = (H_x, H_y, H_z) = (H^+ + H^{-*}, -iH^+ + iH^{-*}, H_z)$ [36]. It is assumed in the forthcoming that H^+ can be measured by MRI techniques and therefore it is desired to obtain a relation between H^+ and γ. (H^- cannot be measured using MRI since it is counter productive in MRI).

Admittivity appears in Ampere's Law (with Maxwell's correction) as $\nabla \times \mathbf{H} =$

$\gamma\mathbf{E}$. By taking the curl of both sides of this equation, by using the fact that $\nabla\cdot\mathbf{H} = 0$, and also by making use of the vector identity $\nabla \times \nabla \times \mathbf{H} = -\nabla^2\mathbf{H} + \nabla\nabla \cdot \mathbf{H}$ and the Faraday's Law $\nabla \times \mathbf{E} = -i\omega\mu\mathbf{H}$, we can obtain an equation involving the magnetic field only, as follows:

$$\nabla \times \nabla \times \mathbf{H} = \nabla \times (\gamma\mathbf{E}) = \nabla\gamma \times \mathbf{E} + \gamma\nabla \times \mathbf{E} \tag{2.1}$$

$$\Rightarrow\ -\nabla^2\mathbf{H} = \frac{\nabla\gamma}{\gamma} \times (\nabla \times \mathbf{H}) - i\omega\mu\gamma\mathbf{H} \tag{2.2}$$

We can write the x- and y-components of Equation (2.2) as:

$$-\nabla^2 H_{\mathrm{x}} = \frac{1}{\gamma}\frac{\partial\gamma}{\partial y}\left(\frac{\partial H_{\mathrm{y}}}{\partial \mathrm{x}} - \frac{\partial H_{\mathrm{x}}}{\partial \mathrm{y}}\right) - \frac{1}{\gamma}\frac{\partial\gamma}{\partial z}\left(\frac{\partial H_{\mathrm{x}}}{\partial \mathrm{z}} - \frac{\partial H_{\mathrm{z}}}{\partial \mathrm{x}}\right) - i\omega\mu\gamma H_x \tag{2.3}$$

$$-\nabla^2 H_{\mathrm{y}} = \frac{1}{\gamma}\frac{\partial\gamma}{\partial z}\left(\frac{\partial H_{\mathrm{z}}}{\partial \mathrm{y}} - \frac{\partial H_{\mathrm{y}}}{\partial \mathrm{z}}\right) - \frac{1}{\gamma}\frac{\partial\gamma}{\partial x}\left(\frac{\partial H_{\mathrm{y}}}{\partial \mathrm{x}} - \frac{\partial H_{\mathrm{x}}}{\partial \mathrm{y}}\right) - iw\mu\gamma H_y \tag{2.4}$$

If we multiply Equation (2.4) by i and add to Equation (2.3), we obtain

$$\begin{aligned} -2\nabla^2 H^+ \ &= \ -\frac{1}{\gamma}\frac{\partial\gamma}{\partial x} i\left(\frac{\partial H_y}{\partial x} - \frac{\partial H_x}{\partial y}\right) - \frac{1}{\gamma}\frac{\partial\gamma}{\partial y}\left(-\frac{\partial H_y}{\partial x} + \frac{\partial H_x}{\partial y}\right) \\ &\quad -\frac{1}{\gamma}\frac{\partial\gamma}{\partial z}\left[2\frac{\partial H^+}{\partial z} - \frac{\partial H_z}{\partial x} - i\frac{\partial H_z}{\partial y}\right] - 2i\omega\mu\gamma H^+ \end{aligned} \tag{2.5}$$

By using the definitions of H^+, H^-, and $\nabla \cdot \mathbf{H} = \frac{\partial H_x}{\partial x} + \frac{\partial H_y}{\partial y} + \frac{\partial H_z}{\partial z} = 0$ we can modify the $\left(\frac{\partial H_{\mathrm{y}}}{\partial \mathrm{x}} - \frac{\partial H_{\mathrm{x}}}{\partial \mathrm{y}}\right)$ factor as

$$\begin{aligned} \frac{\partial H_{\mathrm{y}}}{\partial \mathrm{x}} - \frac{\partial H_{\mathrm{x}}}{\partial \mathrm{y}} \ &= \ \frac{\partial H_{\mathrm{y}}}{\partial \mathrm{x}} - \frac{\partial H_{\mathrm{x}}}{\partial \mathrm{y}} - i\left(\frac{\partial H_x}{\partial x} + \frac{\partial H_y}{\partial y} + \frac{\partial H_z}{\partial z}\right) \\ &= \ 2i\left(-i\frac{\partial H^+}{\partial x} - \frac{\partial H^+}{\partial y} - \frac{i}{2}\frac{\partial H_z}{\partial z}\right) - i\frac{\partial H_z}{\partial z} \end{aligned} \tag{2.6}$$

By using this identity, Equation (2.5) becomes:

$$\begin{aligned} -\nabla^2 H^+ \ &= \ -\frac{1}{\gamma}\frac{\partial\gamma}{\partial x}\left(\left(\frac{\partial H^+}{\partial x} - i\frac{\partial H^+}{\partial y}\right) + \frac{1}{2}\frac{\partial H_z}{\partial z}\right) \\ &\quad -\frac{1}{\gamma}\frac{\partial\gamma}{\partial y}\left(i\left(\frac{\partial H^+}{\partial x} - i\frac{\partial H^+}{\partial y}\right) + \frac{i}{2}\frac{\partial H_z}{\partial z}\right) \\ &\quad -\frac{1}{\gamma}\frac{\partial\gamma}{\partial z}\left(\frac{\partial H^+}{\partial z} - \frac{1}{2}\frac{\partial H_z}{\partial x} - \frac{i}{2}\frac{\partial H_z}{\partial y}\right) - i\omega\mu\gamma H^+ \end{aligned} \tag{2.7}$$

Dividing by γ and using the definition $u = 1/\gamma$, Equation (2.7) can be written as:

$$\mathbf{C} \cdot \nabla u + \nabla^2 H^+ u - i\omega\mu H^+ = 0 \tag{2.8}$$

where

$$\nabla u = \begin{bmatrix} \dfrac{\partial u}{\partial x} \\ \dfrac{\partial u}{\partial y} \\ \dfrac{\partial u}{\partial z} \end{bmatrix} = \begin{bmatrix} -\dfrac{1}{\gamma^2}\dfrac{\partial \gamma}{\partial x} \\ -\dfrac{1}{\gamma^2}\dfrac{\partial \gamma}{\partial y} \\ -\dfrac{1}{\gamma^2}\dfrac{\partial \gamma}{\partial z} \end{bmatrix} \text{ and } \mathbf{C} = \begin{bmatrix} C_x \\ C_y \\ C_z \end{bmatrix} = \begin{bmatrix} \dfrac{\partial H^+}{\partial x} - i\dfrac{\partial H^+}{\partial y} + \dfrac{1}{2}\dfrac{\partial H_z}{\partial z} \\ i\dfrac{\partial H^+}{\partial x} + \dfrac{\partial H^+}{\partial y} + \dfrac{i}{2}\dfrac{\partial H_z}{\partial z} \\ \dfrac{\partial H^+}{\partial z} - \dfrac{1}{2}\dfrac{\partial H_z}{\partial x} - \dfrac{i}{2}\dfrac{\partial H_z}{\partial y} \end{bmatrix}$$

This equation is the well-known convection-diffusion-reaction equation with null diffusion term, where $\mathbf{C}$ is the convective field and $\nabla^2 H^+ u - i\omega\mu H^+$ is the reaction component [37]. (Note that $C_y = iC_x$)

We have already assumed that H^+ can be measured using MRI. If additionally the gradient of H_z is known, then Equation (2.8) can be solved in three dimensions for u by imposing appropriate boundary conditions. However, measurement of H_z component is not feasible in MRI. On the other hand, H_z can be neglected in the central regions for a birdcage RF coil where end-ring generated H_z field is minimum. In many reconstruction applications, u is desired to be found in a specified xy-plane (slice). For such applications, if it can be assumed that $\partial u/\partial z$ is negligible for the slice of interest then Equation (2.8) can be simplified into its 2-D form:

$$\mathbf{F} \cdot \bar{\nabla} u + \nabla^2 H^+ u - i\omega\mu H^+ = 0 \tag{2.9}$$

where $\bar{\nabla} u = \begin{bmatrix} \dfrac{\partial u}{\partial x} \\ \dfrac{\partial u}{\partial y} \end{bmatrix}$ and $\mathbf{F} = \begin{bmatrix} F_x \\ F_y \end{bmatrix} = \begin{bmatrix} \dfrac{\partial H^+}{\partial x} - i\dfrac{\partial H^+}{\partial y} \\ i\dfrac{\partial H^+}{\partial x} + \dfrac{\partial H^+}{\partial y} \end{bmatrix}$.

If $\bar{\nabla} u$ is assumed to be negligible such as in regions where electrical properties vary slowly, then the solution of Equation (2.9) reduces to

$$u = \frac{i\omega\mu H^+}{\nabla^2 H^+} \tag{2.10}$$

This formula is in effect the same as the Wen's formula mentioned in Chapter 1.2 except that $u = 1/\gamma$. (Note that the symbol H^+ used in this section and the symbol B_1^+ used frequently in the literature both represent the left-handed rotating RF field and that $B_1^+ = \mu H^+$.)

From MRI system, B_1^+ can be measured and so H^+ can be found using the relation, $H^+ = B_1^+/\mu$, where μ is the magnetic permeability. The magnetic permeability, μ is given by

$$\mu = \mu_0 (1 + \chi_v) \tag{2.11}$$

where χ_v is volume magnetic susceptibility. Water is the predominant component of most tissues and the susceptibility of most tissues appears to be within $\pm 10\% - 20\%$ that of water; i.e., $\chi_{water} = -9.05 \times 10^{-6}$ and $-11 \times 10^{-6} < \chi_{tissue} < -7 \times 10^{-6}$ [38]. For example, the magnetic susceptibility values of bone and whole blood are $\chi_{bone} = -11.31 \times 10^{-6}$ and $\chi_{blood} = -7.9 \times 10^{-6}$, respectively [38]. Therefore, when the spatial resolution of the MRI images is considered, the first and second derivatives of the magnetic permeability for tissues can be neglected in our formulas. In other words, the magnetic permeability of tissues can be assumed to be constant and equal to the magnetic permeability of the free space, $\mu = \mu_0 = 4\pi \times 10^{-7}$. All MREPT algorithms use this assumption [39].

The coefficients of the partial differential equation in Equation (2.9) depend on H^+ and therefore H^+ must be measured. Magnitude of H^+ can be found by one of the several available B_1 mapping techniques [30][32][40]-[42]. In this thesis we have used the double-angle-method [30]. For the measurement of the phase of H^+ no exact and general method has been developed so far. However, as explained in Section 3.3.2 the phase of H^+ can be closely estimated if a quadrature birdcage RF coil is used [25].

Chapter 3

Methods

3.1 Solution of the Convection-Reaction Equation based MREPT (cr-MREPT)

3.1.1 Convection-Reaction Equation based MREPT (cr-MREPT) using a Triangular Mesh based Finite Difference Method

In cr-MREPT method, in order to reconstruct σ and ε, Equation (2.9) is solved for u. A triangular mesh based finite difference method is proposed where a triangular mesh is generated in the imaging slice as a first step. It is assumed that H^+ is measured (known) on the nodes of the triangular mesh. The procedure for obtaining H^+ distribution on the nodes from the MR raw data is discussed in the "Experimental Methods" section. Equation (2.9), which is a partial differential equation, has the first derivatives and the Laplacian of H^+ as its space dependent coefficients. In the following, it is assumed that these coefficients are already calculated on the nodes (the procedure for calculating these first derivatives and the Laplacian is discussed at the end of this section).

Inside each triangular element, u can be approximated as

$$u(x,y) = \sum_{i=1}^{3} u_{i,j}\phi_{i,j}(x,y) \qquad (x,y) \in \Omega_j \ , \ j = 1,\ 2,\ ...,\ \mathrm{N}_t \tag{3.1}$$

where Ω_j denotes the inside of the j'th triangle, N_t is the number of triangles in the imaging slice, $u_{i,j}$ is the value of u at the i'th node of the j'th triangle, and $\phi_{i,j}(x,y) = a_{i,j}x + b_{i,j}y + c$. In the finite element method (FEM) literature, $\phi_{i,j}(x,y)$ is called linear shape function. The coefficients, a, b, and c, in these equations can be calculated by using the definitions $\phi_{i,j}(x_{m,j}, y_{m,j}) = 1$ if $i = m$ and $\phi_{i,j}(x_{m,j}, y_{m,j}) = 0$ otherwise where $(x_{m,j}, y_{m,j})$ are the coordinates of the m'th node of the j'th triangle $(i, m = 1, 2, 3)$. Once the coefficients are determined, $\partial u/\partial x$ and $\partial u/\partial y$ are found inside the j'th triangle as follows

$$\frac{\partial u(x,y)}{\partial x} = \sum_{i=1}^{3} u_{i,j}a_{i,j} \quad \text{and} \quad \frac{\partial u(x,y)}{\partial y} = \sum_{i=1}^{3} u_{i,j}b_{i,j} \tag{3.2}$$

Similar to how u is approximated in Equation (3.1), each of F_x, F_y and $\nabla^2 H^+$ can also be approximated in a triangle using their nodal values and the linear shape functions. Using these approximations and also Equation (3.2), Equation (2.9) can be written for each triangle as

$$\begin{aligned} &\sum_{i=1}^{3} F^x_{i,j}\phi_{i,j}(x,y) \sum_{i=1}^{3} u_{i,j}a_{i,j} + \sum_{i=1}^{3} F^y_{i,j}\phi_{i,j}(x,y) \sum_{i=1}^{3} u_{i,j}b_{i,j} \\ &+ \sum_{i=1}^{3} \nabla^2 H^+_{i,j}\phi_{i,j}(x,y) \sum_{i=1}^{3} u_{i,j}\phi_{i,j}(x,y) = i\omega\mu \sum_{i=1}^{3} H^+_{i,j}\phi_{i,j}(x,y) \end{aligned} \tag{3.3}$$

where $F^x_{i,j}$, $F^y_{i,j}$, $\nabla^2 H^+_{i,j}$, and $H^+_{i,j}$ are F_x, F_y, $\nabla^2 H^+$ and H^+ values at the i'th node of the j'th triangle, respectively. Evaluating Equation (3.3) at the centroid of the j'th triangle, denoted by (x_j, y_j), and rearranging terms, one obtains

$$\sum_{i=1}^{3} u_{i,j} \left(a_{i,j}F^x_j + b_{i,j}F^y_j + \nabla^2 H^+_j \right) = i\omega\mu H^+_j \tag{3.4}$$

where F^x_j, F^y_j, $\nabla^2 H^+_j$, and H^+_j are defined at the centroid of the j'th triangle and they are the means of the three corresponding nodal values (note that $F^x_j = \sum_{i=1}^{3} F^x_{i,j}\phi_{i,j}(x_j, y_j) = \sum_{i=1}^{3} F^x_{i,j}/3$ and similarly for F^y_j, $\nabla^2 H^+_j$, and H^+_j). Assigning

global indices to all nodes in the imaging slice, Equation (3.4) is written for the j'th triangle as

$$\sum_k u_k \left(a_k F_j^x + b_k F_j^y + \nabla^2 H_j^+ \right) = i\omega\mu H_j^+ \tag{3.5}$$

where $k \in P_j$ and P_j by definition contains three integers which are the global indices of the nodes of the j'th triangle. Equation (3.5) can be written for each triangle and a matrix system is obtained as

$$\mathbf{K}_{\mathrm{N}_t \mathrm{x} \mathrm{N}_p} \mathbf{u}_{\mathrm{N}_p \mathrm{x} 1} = \mathbf{f}_{\mathrm{N}_t \mathrm{x} 1} \tag{3.6}$$

where N_t is the number of triangles and N_p is the number of nodes on the imaging slice. Note that each row of the $\mathbf{K}$ matrix has only three non-zero elements. For the solution of Equation (2.9), boundary conditions should also be considered. In cr-MREPT method, u values at the boundaries of the solution domain are assumed to be known (i.e. Dirichlet boundary condition is used). This information is used to eliminate corresponding columns of the matrix $\mathbf{K}$ and the number of unknowns (N_p) is decreased. Since $\mathrm{N}_t > \mathrm{N}_p$, the system is over-determined and it is solved in the least-square sense.

As discussed in "Simulation Results" section, in some cases, it is desired to specify u values in a certain region and use this information as a-priori knowledge (as a constraint). The u values in this region are calculated beforehand whether using another reconstruction method or they are assumed to be known. Similar to the boundary nodes, this information is incorporated in the solution by eliminating corresponding columns of the matrix $\mathbf{K}$ and the number of unknowns (N_p) is further decreased.

As discussed above, $\mathbf{K}$ matrix and $\mathbf{f}$ vector in Equation (3.6) are constructed using the measured data and thus they are strictly related to the distribution of H^+. Obviously, for different H^+ distributions, different $\mathbf{K}$ and $\mathbf{f}$ are obtained. Let $\mathbf{K_1}$, $\mathbf{K_2}$ and $\mathbf{f_1}$, $\mathbf{f_2}$ be obtained for two different H^+ distributions. In this case, these matrices and vectors can be concatenated for the solution of u as follows:

$$\left[\begin{array}{c} \mathbf{K_1} \\ \mathbf{K_2} \end{array} \right]_{2\mathrm{N}_t \mathrm{x} \mathrm{N}_p} \mathbf{u}_{\mathrm{N_P x 1}} = \left[\begin{array}{c} \mathbf{f_1} \\ \mathbf{f_2} \end{array} \right]_{2\mathrm{N}_t \mathrm{x} 1} \tag{3.7}$$

Similar to the case when Equation (3.6) is solved alone, the boundary conditions and the a-priori knowledge (if desired) are used to eliminate corresponding

columns of the concatenated matrix in Equation (3.7) and the number of unknowns is decreased. The final matrix system is also over-determined and it is solved in the least-square sense. In the "Simulation Results" section, the rationale behind using two RF excitations resulting in two different H^+ distributions rather than a single excitation is discussed.

3.1.2 Calculation of the First Derivatives and the Laplacian of H^+ at the Triangular Mesh Nodes

For the calculation of the first derivatives and the Laplacian of H^+ at the mesh nodes the method proposed by Fernandez *et al* is used [43]. It is assumed that H^+ is known at the nodes of the triangular mesh defined in the imaging slice. Using nodal H^+ values, the first derivatives and the Laplacian of H^+ are calculated separately for every node as follows: Let n_0 denote the node where the first derivatives and the Laplacian of H^+ are to be calculated and let n_1 to n_6 denote the neighboring nodes of the central node n_0 as shown in Figure 3.1. H^+ is approximated as a second order polynomial in the shaded region as $H^+(x, y) = ax^2 + by^2 + cxy + dx + ey + f$. To find the coefficients, a, b, c, d, e, and f the following set of equations is written:

$$H^+(x_i, y_i) = ax_i^2 + by_i^2 + cx_iy_i + dx_i + ey_i + f \quad \text{for } i = 0, 1, \ldots, 6 \tag{3.8}$$

where x_i and y_i are the x- and y- coordinates of node i. Note that in this system there are 6 unknowns and 7 equations, and therefore the system is solved in the least square sense. However, for some nodes, such as the boundary nodes, the number of equations is less than 6. In such a case, the minimum-norm solution is used for finding the coefficients. Once the coefficients of the second order polynomial are determined, the first derivatives and the 2-D Laplacian of H^+ for node n_0 are found as

$$\frac{\partial H^+}{\partial x} = 2ax_0 + cy_0 + d, \quad \frac{\partial H^+}{\partial y} = 2by_0 + cx_0 + e, \quad \text{and} \quad \bar{\nabla}^2 H^+ = 2a + 2b \tag{3.9}$$

where x_0 and y_0 are the x- and y- coordinates of node n_0. This procedure is repeated for every node of the triangular mesh.

It should be noted that $\nabla^2 H^+$ also involves the second derivative of H^+ with respect to z. In simulations, H^+ is calculated on two other slices one 5 mm above the imaging slice and one 5 mm below the imaging slice. In the experiments, H^+ is measured also on three slices with 5 mm spacing. Therefore, the second derivative with respect to z is calculated using central difference approximation.

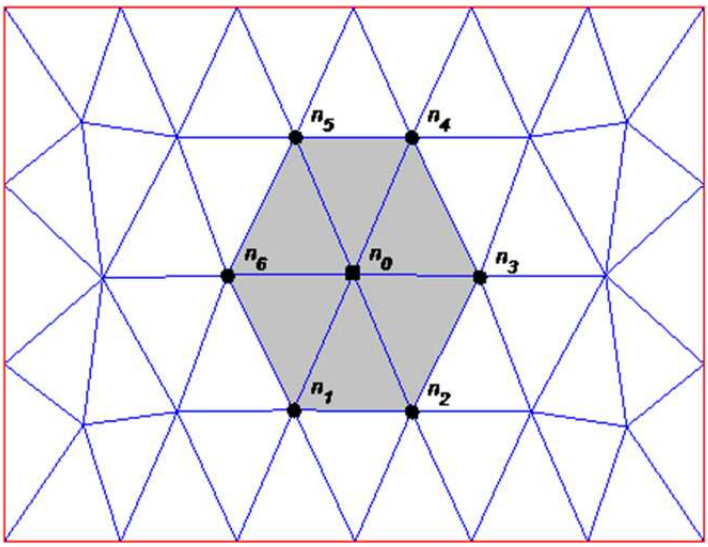

Figure 3.1: A sample region of the triangular mesh at the imaging slice: n_0 and its 6 neighboring nodes (n_1 to n_6) are shown. H^+ is approximated as a second order polynomial in the shaded region using the H^+ values at the nodes n_0 to n_6.

3.2 Simulation Methods

To test the proposed algorithms, simulated data are obtained using MATLAB (The Mathworks, Natick, USA), and COMSOL Multiphysics 4.2a (COMSOL AB, Stockholm, Sweden), a FEM based software package. MATLAB and COMSOL Multiphysics are also used for the implementation of reconstruction algorithms, filters, pre-processing steps, and all numerical procedures.

3.2.1 Birdcage Coil FEM Model

The geometry of the shielded high-pass quadrature birdcage coil which is built in COMSOL Multiphysics is shown in Figure 3.2(a).

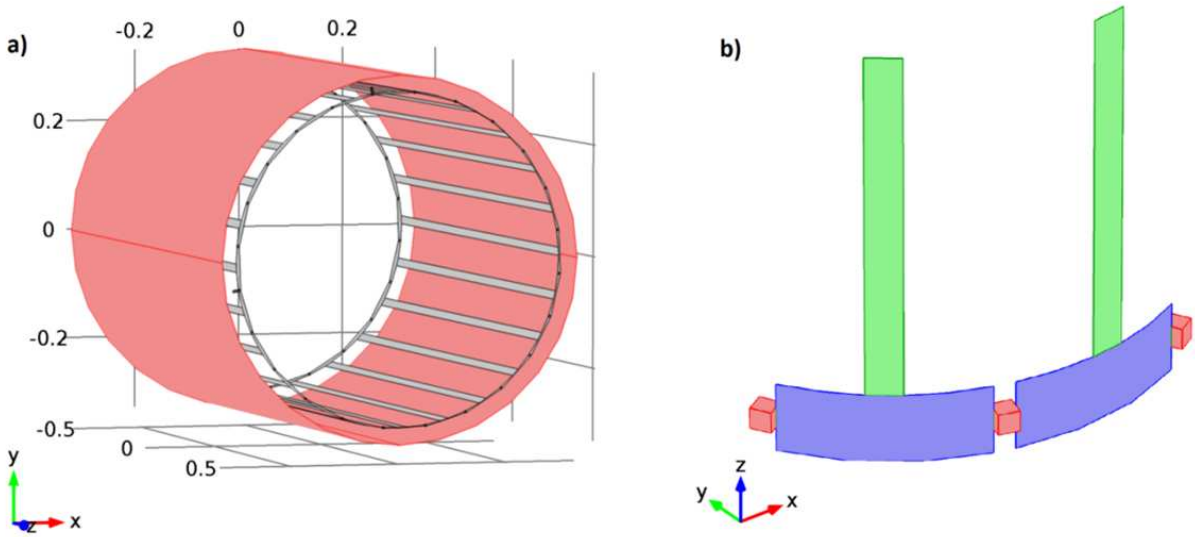

Figure 3.2: (a) A shielded high-pass quadrature birdcage coil model (shield is shown as red) (b) Model of the rungs (green), end rings (purple), and capacitors (red) of the coil.

As shown in Figure 3.2(a), the coil is a 24-leg high-pass birdcage coil with a radius of 0.3 m and length of 1 m. Capacitors (Figure 3.2(b)) in the end rings are modelled as parallel plate capacitors (in 3-D) whereas rungs, and end rings (Figure 3.2(b)) are modelled as rectangular surfaces and Perfect Electric Conductor (PEC) boundary condition is assigned to the surfaces. In order to prevent reflections from the outer boundary of the spherical solution domain of radius 1.5 m, a perfectly matched layer is introduced on the outer boundary [44]. Detailed analysis and modelling of the birdcage coil are given in [45]. In order to generate a homogeneous and circularly polarized H^+ in the region of interest, for the unloaded case, optimum capacitance value is calculated as 8.6 pF at 123.2 MHz (corresponding to the 2.89 T MRI system used in this study) using the method proposed in [46].

3.2.2 Verification of the Coil Model

Calculated $|H^+|$ and $|H^-|$ distributions at the central slice of unloaded quadrature birdcage model at the desired frequency are shown in Figure 3.3. As expected,

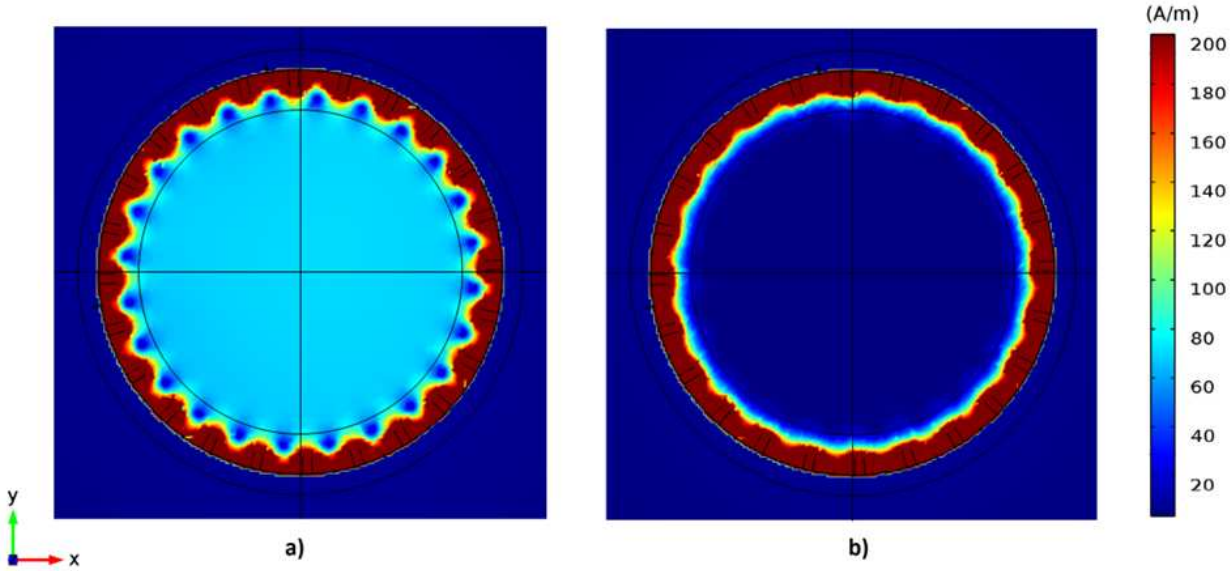

Figure 3.3: (a) $|H^+|$ distribution and (b) $|H^-|$ distribution at the central slice ($z = 0$), when the unloaded quadrature birdcage coil is driven by 500V peak from the ports that are geometrically 90° apart from each other and with 90° phase difference.

$|H^+|$ has uniform distribution whereas $|H^-|$ is nearly zero in the central region of the birdcage coil. Variation of $|H^+|$ is less than $\pm 2\%$ within a cylindrical region of 30 cm length along the z-axis and 30 cm in diameter. Magnetic field distributions for loaded birdcage coil will be given in the simulation results section.

3.2.3 Simulation Phantoms

As the loading objects, two different phantoms shown in Figure 3.4 are modeled in the simulation environment.

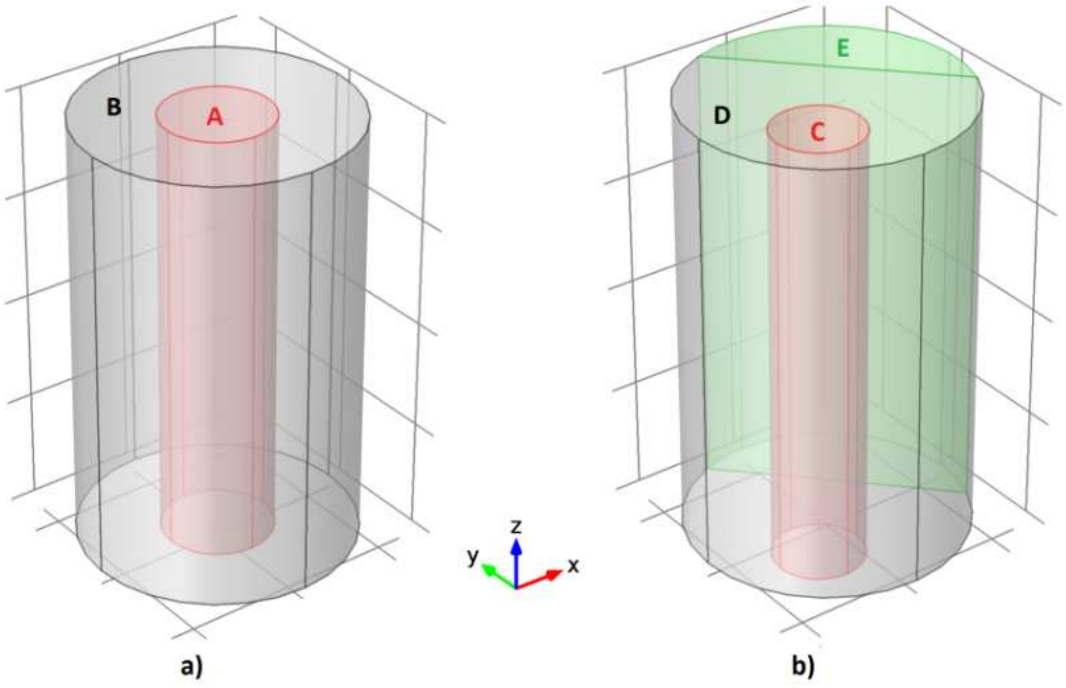

Figure 3.4: (a) The first simulation phantom: geometric model of two concentric cylindrical objects. (b) The second simulation phantom: geometric model of two eccentric cylindrical objects.

The first phantom shown in Figure 3.4(a), called the "first simulation phantom", consists of two concentric cylindrical objects (A and B) with a total diameter of 14.4 cm and a height of 19.5 cm. Object A has a diameter of 7.5 cm and these two objects have different conductivity and permittivity distributions which will be given in the simulation results section.

The second phantom shown in Figure 3.4(b), called the "second simulation phantom", on the other hand, consists of two eccentric cylindrical objects (C and union of D an E) with a total diameter of 14.4 cm and a height of 19.5 cm. Object C has a diameter of 5 cm. The outer cylindrical object is separated into two objects (D and E). This separation provides the possibility of making electromagnetic simulations with and without object E (region E is cut out when so desired) and thus acquiring two different simulated data in the region of interest (D and C).

3.3 Experimental Methods

In order to test the proposed cr-MREPT algorithm with experimental data, two experimental setups are prepared. For these setups, the simulation phantoms shown in Figure 3.4(a) and (b) are manufactured from plexiglass and these are called the "first experimental phantom" and the "second experimental phantom", respectively.

3.3.1 Phantom Preparation

For the first experimental phantom, the background (region B in 3.4(a)) is made by using an agar solution (20 gr/l Agar, 2 gr/l NaCl, 1.5 gr/l $CuSO_4$). NaCl is used for adjusting the conductivity of the phantom and $CuSO_4$ is used for decreasing T_1 of the solution to around 300 *ms*. After region B is solidified (within several hours), region A (shown in Figure 3.4(a)) is filled with a solution of different conductivity (6 gr/l NaCl, 1.5 gr/l $CuSO_4$) in order to obtain conductivity contrast. Since NaCl diffusion between region A and B affects the conductivity distribution, the data acquisition is started right after region A is filled.

The second experimental phantom is prepared by applying similar steps as above: Regions D and E in Figure 3.4(b) are built using an agar solution (20 gr/l Agar, 2 gr/l NaCl, 1.5 gr/l $CuSO_4$) and region C is filled with a solution of different conductivity (6 gr/l NaCl, 1.5 gr/l $CuSO_4$). As discussed in the "Experimental Results" section, two different experiments, with and without region E, are performed using this phantom in order to obtain different H^+ distributions.

It can be deduced from the experimental work of Iizuka that addition of 2% Agar does not significantly alter the electrical properties of our solutions [30]. Therefore, the electrical properties of our solutions are determined by NaCl and to a less extent by $CuSO_4$ (because $CuSO_4$ is used in small amounts). Electrical conductivity was measured at low frequency by a conductivity meter (Hanna Instruments, HI 8733) and similarity with corresponding literature values is observed [47]. Dielectric permittivity of the saline solutions, on the other hand,

was only estimated by the formula given in [47]. In conclusion, for the inner object and the background, we estimate the conductivities to be 1.0 S/m and 0.42 S/m, and the relative permittivities to be 76.3 and 77.6 respectively. From [47], it can be also calculated that salt-free water has a relative permittivity of 80. Moreover, the electrical properties of the solutions at MR RF frequency can be measured using a dielectric spectroscopy which measures the dielectric properties of a medium as a function of frequency [48]. Although we have not measured the electrical properties of our solutions at the MR RF frequency, we think that the above estimates give insight for the relative differences between different solutions and different regions.

3.3.2 Measurement of H^+

3.3.2.1 Measurement of H^+ Magnitude

The magnitude of H^+ can be found by one of the several available B_1 mapping techniques [30][32][40]-[42]. In this thesis, the magnitude of H^+ is measured by using the double-angle method [30]: Two MR magnitude images, $|M_1|$ and $|M_2|$, are acquired by using two gradient-echo pulse sequences of nominal flip angles 60° and 120° respectively. For transmit and receive, the quadrature birdcage body coil of the MRI system is used. The magnitude of H^+ is calculated using the formula

$$\left|H^+\right| = \frac{\cos^{-1}\left(|M_2|/(2\,|M_1|)\right)}{\mu_0 \boldsymbol{\gamma} T_{RF}} \tag{3.10}$$

where T_{RF} is the duration of the RF excitation pulse and $\boldsymbol{\gamma}$ is the gyro-magnetic ratio. The MR imaging parameters are TR = 1500 *ms*, TE = 5 *ms*, FOV = 180 × 180 mm, raw data matrix size = 128×128, number of averages = 5, slice thickness = 5 mm, and number of slices = 8 (no gap). The experiments are conducted using the 3T (nominal) Siemens Magnetom Trio MR scanner installed in UMRAM (National Magnetic Resonance Research Center) at Bilkent University.

3.3.2.2 Measurement of H^+ Phase

For obtaining the phase of H^+, a spin-echo MR image is acquired using the quadrature birdcage body coil of the MRI system. The MR imaging parameters are the same as above except for the nominal flip angle which is chosen to be 90°. The phase of this spin-echo image can be written as

$$\phi_s(\mathbf{r}, T_E) = \phi_{tr}(\mathbf{r}) + \int_0^{T_E} \boldsymbol{\gamma} B_e \mathrm{dt} \tag{3.11}$$

where $\mathbf{r}$ is the position vector, T_E is the echo-time, $\phi_{tr}(r)$ is the transceive phase, and $\int_0^{T_E} \boldsymbol{\gamma} B_e \mathrm{dt}$ is the phase accumulated due to the eddy-currents generated inside the imaging object during the rise-time of the read-out gradient field. $\phi_{tr}(\mathbf{r})$ is the sum of two contributions, namely

$$\phi_{tr}(\mathbf{r}) = \phi_+(\mathbf{r}) + \phi_-(\mathbf{r}) \tag{3.12}$$

where $\phi_+(\mathbf{r})$ and $\phi_-(\mathbf{r})$ are phases due to the RF transmit (excitation) and receive fields respectively. Due to the nature of spin-echo imaging, there is no phase term related to the B_0 field inhomogeneity.

It is a known fact that the polarity of $\int_0^{T_E} \boldsymbol{\gamma} B_e \mathrm{dt}$ term depends on the polarity of the read-out gradient, i.e. if k-space is scanned from $k_{x,\max}$ to $-k_{x,\max}$ rather than from $-k_{x,\max}$ to $k_{x,\max}$, this term changes sign (assuming read-out direction is x). In this thesis, as suggested in [28], this fact is exploited for obtaining $\phi_{tr}(\mathbf{r})$ as follows:
Two phase images are acquired by using spin-echo pulse sequences of different read-out gradient polarities. Their phases are then summed and the resulting phase is halved to obtain $\phi_{tr}(\mathbf{r})$. It is assumed that the transmit and receive phases of a quadrature birdcage coil are very close to each other, i.e. $\phi_+(\mathbf{r}) \approx \phi_-(\mathbf{r})$ [25], and as a result of this assumption, the phase of H^+ is calculated as half of the transceive phase:

$$\phi_+(\mathbf{r}) \approx \phi_{tr}(\mathbf{r})/2 \tag{3.13}$$

The relation between the transmit and transceive phase can be derived using the formalism of Overall *et al* for imperfect quadrature excitation [49]. Two

ports (Q and I) which are placed orthogonally with respect to each other are considered. B_x^I and B_y^Q are the desired main fields generated by ports Q and I. δB_x^Q and δB_y^I are residual fields due to electromagnetic interaction with the sample. If the port Q is phased to lead I by 90° ($I + jQ$), the forward transmit effective field (B_1^+ in transmit mode) is generated:

$$B_1^+ = \frac{1}{2}\left[B_x^I + B_y^Q + j\left(\delta B_x^Q - \delta B_y^I\right)\right] \tag{3.14}$$

If we switch the sign of the port Q to lag I by 90° ($I - jQ$), the forward receive field (B_1^- in receive mode) for quadrature excitation is generated:

$$B_1^- = \frac{1}{2}\left[B_x^I + B_y^Q - j\left(\delta B_x^Q - \delta B_y^I\right)\right] \tag{3.15}$$

Using the Equation (3.14) and (3.15), the transceive field is given by:

$$B_1^+ B_1^- = \frac{1}{4}\left[\left(B_x^I + B_y^Q\right)^2 + \left(\delta B_x^Q - \delta B_y^I\right)^2\right] \tag{3.16}$$

If $\delta B_x^Q - \delta B_y^I = 0$, the B_1^+ and transceive field simplify to:

$$B_1^+ = \frac{1}{2}\left[B_x^I + B_y^Q\right] \tag{3.17}$$

$$B_1^+ B_1^- = \frac{1}{4}\left[\left(B_x^I + B_y^Q\right)^2\right] \tag{3.18}$$

Thus, the B_1^+ phase(ϕ_+) and the transceive phase (ϕ_{tr}) are, respectively:

$$\phi_+ = \arg\left[B_x^I + B_y^Q\right] \tag{3.19}$$

$$\phi_{tr} = \arg\left[\left(B_x^I + B_y^Q\right)^2\right] = 2\arg\left[B_x^I + B_y^Q\right] = 2\phi_+ \tag{3.20}$$

The condition, $\delta B_x^Q - \delta B_y^I = 0$, is satisfied, when the residual fields can be neglected (i.e. $\delta B_x^Q \approx 0$ and $\delta B_y^I \approx 0$) or when the residual fields are approximately equal ($\delta B_x^Q \approx \delta B_y^I$). In the case of unloaded quadrature birdcage coil, the residual fields are zero, as a consequence, the condition is satisfied. Furthermore, it can be argued that the residual fields are equal in several situations, e.g., circular symmetry [28].

By van Lier *et al.*, the feasibility, validity and precision of this measurement method of B_1^+ phase were demonstrated in cylindrical phantoms and in vivo in the human head [28]. Since cr-MREPT method based on this measurement method of B_1^+ phase, cr-MREPT method gives more accurate results when this measurement method is more accurate.

3.3.3 Obtaining H^+ on the Nodes of the Triangular Mesh

As discussed above, the proposed cr-MREPT algorithm is triangular mesh based and it is required that H^+ is known on the nodes of the triangular mesh in the imaging slice. In order to obtain H^+ on the nodes of the triangular mesh, it is necessary that M_1, M_2, and the spin-echo MR images are reconstructed on the nodes as well. These MR images are obtained on the nodes from the corresponding raw (fid) data matrices by evaluating the inverse discrete Fourier transform at the nodes: The value of a complex MR image at the k'th node, $m(k)$, can be expressed as

$$m(k) = \frac{1}{N^2} \sum_{u=1}^{N} \sum_{v=1}^{N} s(u,v) e^{i2\pi\Delta k(vx_k + uy_k)} \qquad k = 1, 2, ..., N_p \tag{3.21}$$

where $s(u,v)$ denotes the raw data matrix, Δk denotes the spatial frequency spacing in x- and y- directions ($\Delta k = 1/FOV$), x_k and y_k denote the x- and y-coordinates of the k'th node, N denotes the raw data matrix size, and N_p denotes the number of nodes in the imaging slice.

Chapter 4

Results

4.1 Simulation Results

In this section, we first present simulation results for the first simulation phantom. The actual conductivity and permittivity distributions of this phantom which has two concentric cylinders is shown in Figure 4.2(a) and 4.3(a). It should be noted that in this phantom material properties do not change in the z-direction and furthermore in the internal boundaries the material properties change in a tapered fashion (not abruptly). The central slice ($z = 0$) of the phantom is chosen as the slice of interest, and the corresponding H^+ magnitude, and H^+ phase distributions are shown in Figure 4.1(a) and (b). $\nabla^2 H^+$ distribution, and the modulus of the convective field, are shown in Figure 4.1(c) and (d) (Note that since $F_y = iF_x$, $|\mathbf{F}| = \sqrt{\mathbf{F} \cdot \mathbf{F}^*} = \sqrt{2}\,|F_x| = \sqrt{2}\,|F_y|$). It is observed that the modulus of the convective field falls to zero at the center. The $\nabla^2 H^+$ distribution, as expected, has high magnitude on the internal boundaries (transition regions). Using these data, σ and ε distributions are reconstructed by applying both the Wen's method and also the cr-MREPT method that we have proposed.

The reconstructed σ and ε distributions obtained using the Wen's method are shown in Figure 4.2(b) and 4.3(b), respectively. This method gives good reconstruction results in the regions where the spatial variations of σ and ε are

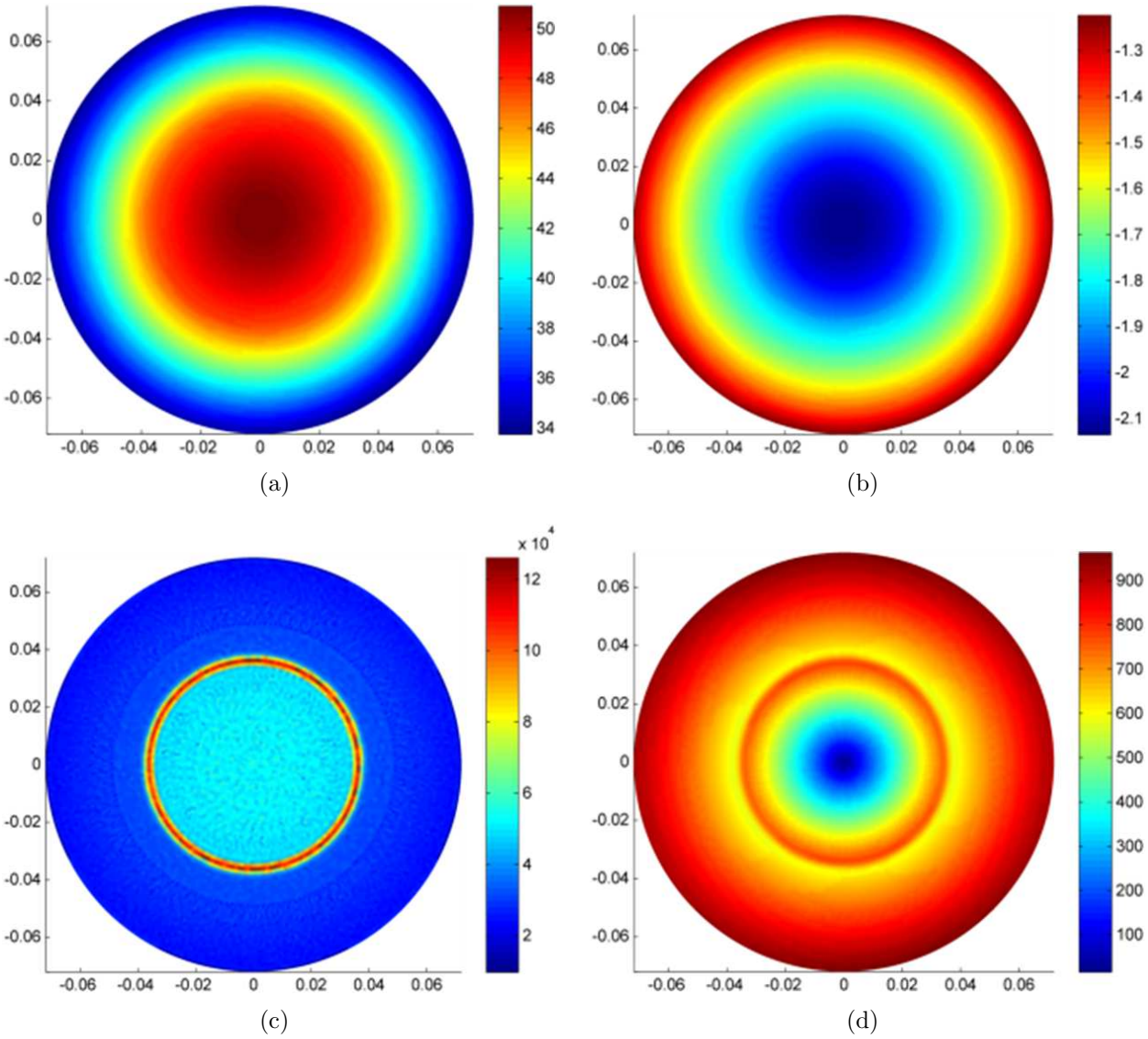

Figure 4.1: Simulation results for the central axial slice of the first simulation phantom: (a) magnitude of H^+, (b) phase of H^+, (c) modulus of $\nabla^2 H^+$, (d) modulus of the convective field. Units are arbitrary. Modulus of the convective field has much lower value at the region around the center of the imaging slice, and this region is called as LCF (Low Convection Field) region.

small but it yields severe errors in and around the boundary (transition) regions. This is because Wen's method assumes that spatial variations of σ and ε are small in the region of reconstruction and the term involving $\bar{\nabla}u = \bar{\nabla}(1/\gamma)$ in Equation (2.9) is not taken into account in this method.

Figure 4.2 and 4.3 also show the results of the cr-MREPT method and the most important advantage of this method seems to be its ability to reliably reconstruct σ and ε distributions everywhere including the transition regions. On the other hand, cr-MREPT method seems to be ill-conditioned (not well-posed) at the origin where a spot-like artifact is observed. This artifact is mainly due to the numerical errors introduced by the region where the modulus of the convective field (in Equation (2.9)) is nearly zero (shown in Figure 4.1(d)). This region is referred to as the Low Convection Field (LCF) region. To eliminate the spot-like artifact, we propose two different methods.

4.1.1 Constrained cr-MREPT

In the first method, called "constrained cr-MREPT", we determine the LCF region by observing the convective field, and in this region we use Wen's method (i.e., Equation (2.10)) which is derived by ignoring the convection term in Equation (2.9). Then, we solve Equation (2.9) by providing the σ and ε found by Wen's method in the LCF region as a-priori knowledge (as explained in Section 3.1). The resultant reconstructed σ and ε distributions, shown in Figure 4.2(d) and 4.3(d), do not have spot-like artifacts. This improvement in the reconstructions is also observed in the line profiles of reconstructed conductivity and permittivity shown in Figure 4.4. However, this method does not give reliable reconstruction results when the LCF region coincides with the boundaries. This is simply because Wen's method gives unreliable estimates of the electrical properties in regions where they vary.

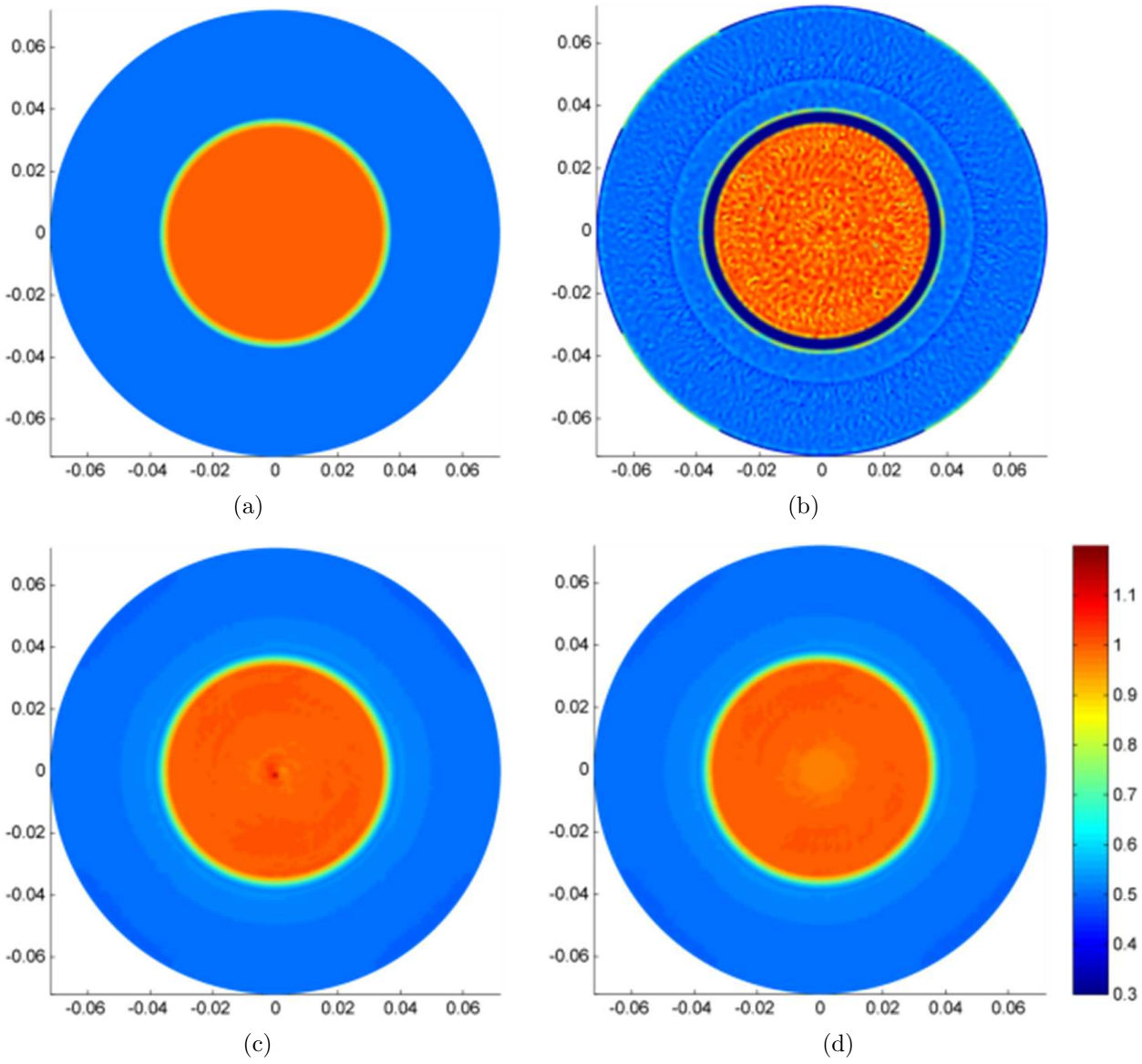

Figure 4.2: Conductivity σ (S/m) reconstruction results for the first simulation phantom: (a) true σ, (b) reconstructed σ using the Wen's method, (c) reconstructed σ using cr-MREPT method, (d) reconstructed σ using the constrained cr-MREPT method. The spot-like artifact observed in (c) at the center is eliminated when constrained cr-MREPT method is used as shown in (d).

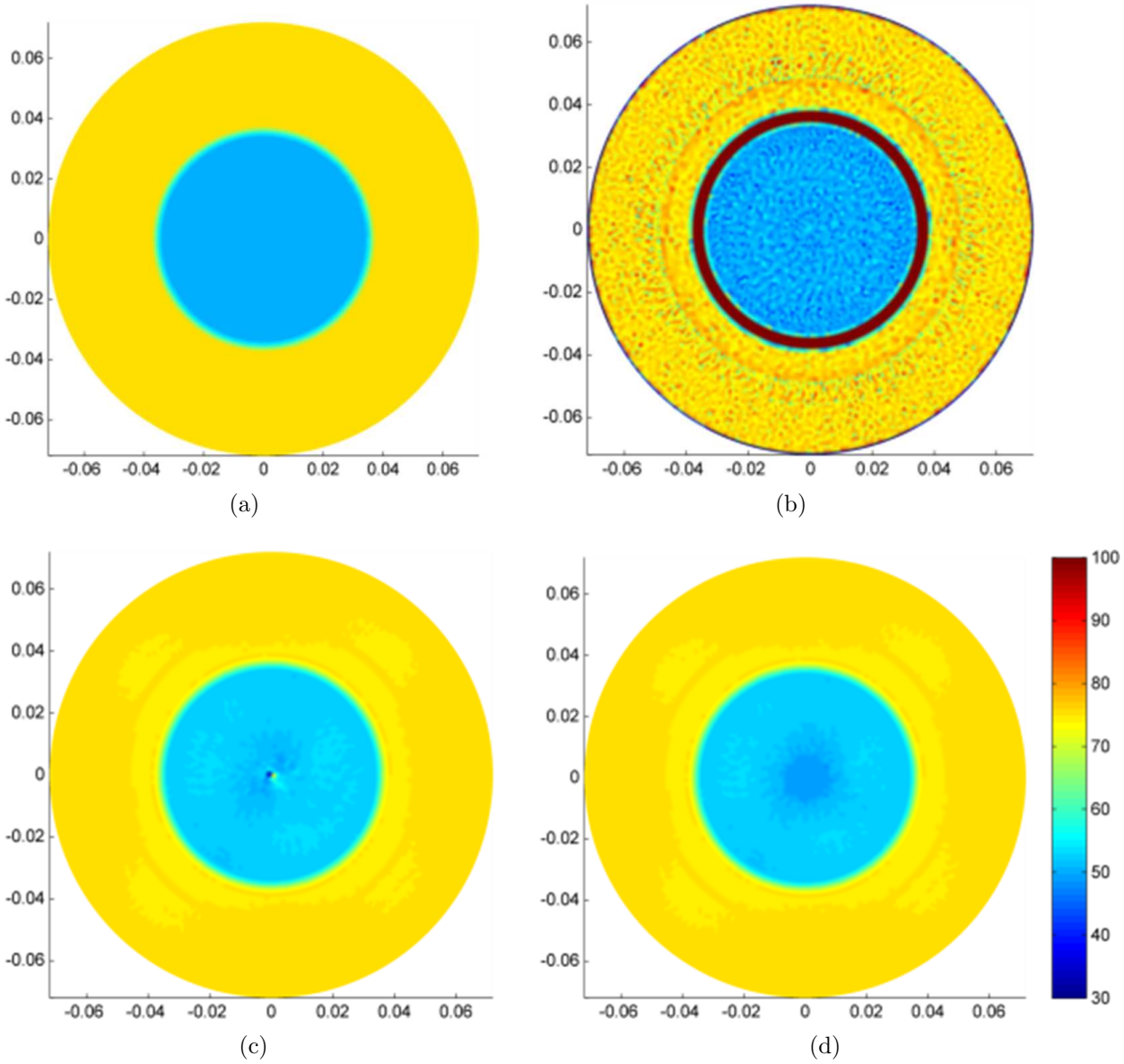

Figure 4.3: Relative dielectric permittivity ε_r reconstruction results for the first simulation phantom: (a) true ε_r, (b) reconstructed ε_r using the Wen's method, (c) reconstructed ε_r using cr-MREPT method, (d) reconstructed ε_r using the constrained cr-MREPT method. The spot-like artifact observed in (c) at the center is also eliminated when constrained cr-MREPT method is used as shown in (d).

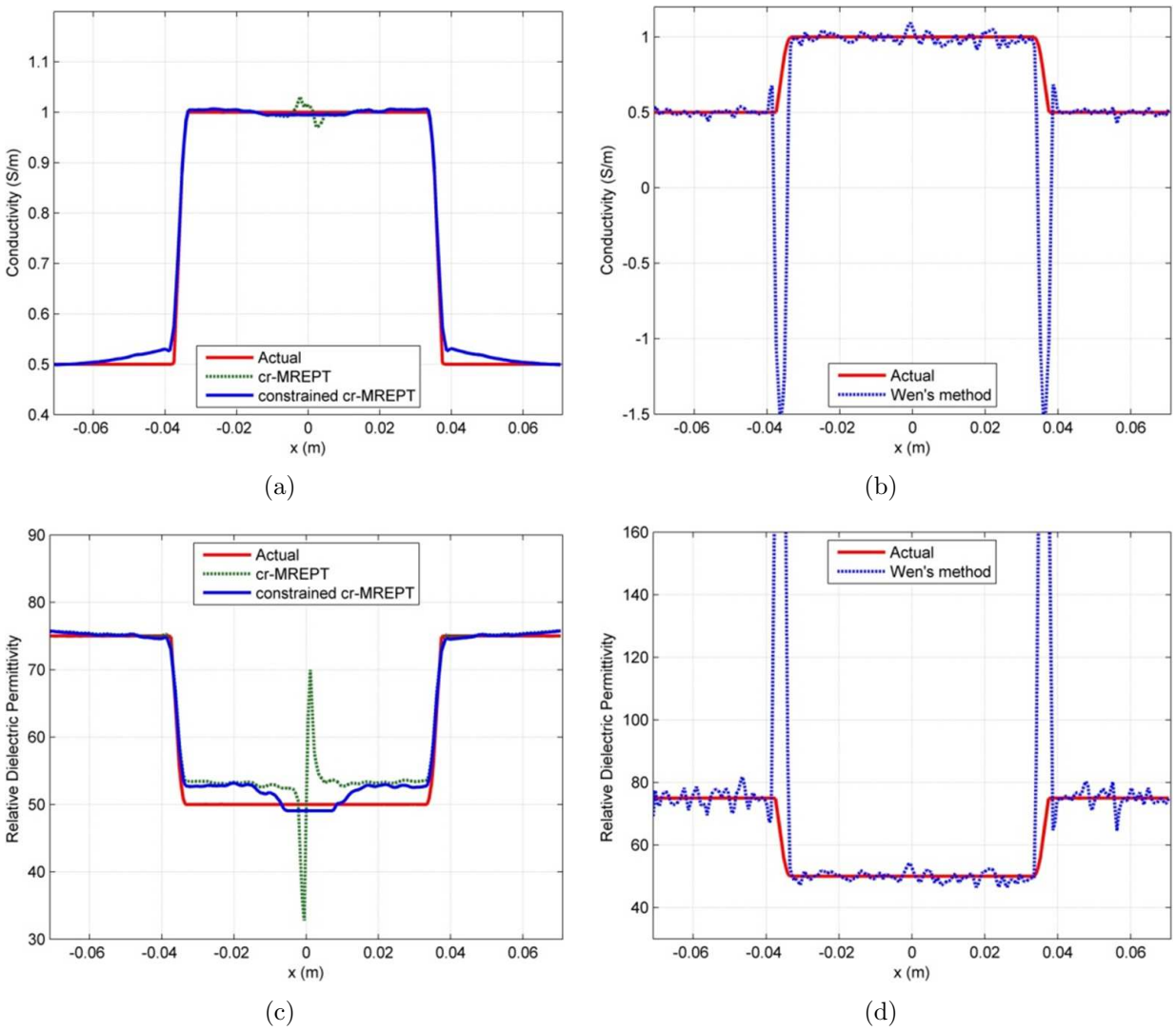

Figure 4.4: Line profiles of the reconstructed and the actual conductivity along the x-axis for the first simulation phantom: (a) The cr-MREPT and the constrained cr-MREPT are used for the reconstruction, (b) Wen's method is used for the reconstruction. (c) and (d) The reconstructed relative dielectric permittivity using the same methods as in (a) and (b). The spot-like artifact observed in cr-MREPT reconstructions is eliminated when constrained cr-MREPT is used.

4.1.2 Double-excitation cr-MREPT

The second method, called "double-excitation cr-MREPT", is reconstructing σ and ε using two different H^+ data that have different LCF regions. To explain and test this method the second simulation phantom shown in Figure 3.4(b) is used. In this phantom there are 3 regions, C, D, and E. Regions D and E are the background regions and region C represents the anomaly region where σ and ε are different. This anomaly region and its immediate surrounding (including the transition region) is our region of interest. We need to realize two different experiments in which the H^+ data in the region of interest are different. This is achieved by including or excluding region E in the simulations. In other words in one case region E is assigned the same material properties as region D, and in the other case it is assumed to be cut out (or assigned material properties of air).

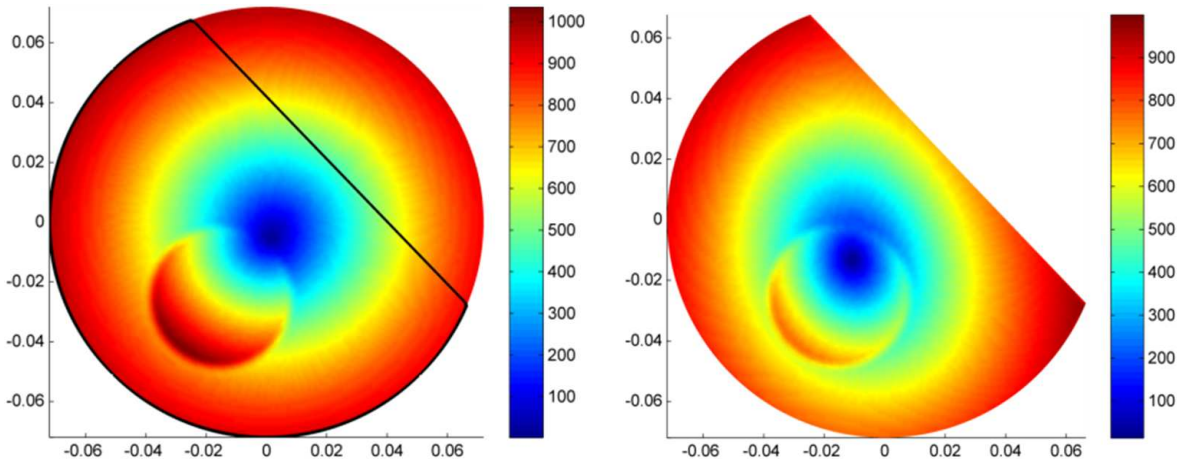

Figure 4.5: Moduli of the convective fields for the second simulation phantom using two different excitations: (a) Region E is included (assigned the same material properties as region D), (b) Region E is cut out (assigned material properties of air). The region of interest (C and D) is enclosed by a black border in (a). Convective fields shown in (a) and (b) have different LCF regions in the region of interest

Using this procedure, we obtain two different H^+ data for the region of interest by modifying the regions external to the region of interest. These two different

H^+ data, that also have different LCF regions in the region of interest, are shown in Figure 4.5(a) and (b). If these H^+ data are used separately for cr-MREPT method, the reconstruction results are obtained as shown in Figure 4.6(a)(b) and 4.7(a)(b) and the spot-like artifacts can be observed in the corresponding LCF regions. Using these H^+ data together, Equation (2.9) is solved via Equation (3.7) and the reconstructed σ and ε, shown in Figure 4.6(c) and 4.7(c), do not have spot-like artifacts. Figure 4.6(d) and 4.7(d) show the reconstruction results of Wen's method when the first H^+ data is used and as in previous results, this method yields severe errors in the transition regions.

4.1.3 Noise Behaviour of cr-MREPT

The noise tolerance of the double-excitation cr-MREPT method is also investigated by using the second simulation phantom. In order to obtain noisy complex H^+ data, the following procedure is applied:

a) Obtaining noisy H^+ magnitude

   i. Simulated $|H^+|$ is obtained

   ii. MR magnitude image with nominal 60° flip angle is obtained using the formula $S_1 = \sin(k\,|H^+|)$. The constant k is determined so that the average flip angle in the imaging slice is 60°. MR magnitude image with nominal 120° flip angle is obtained by the formula $S_2 = \sin(2k\,|H^+|)$.

   iii. An SNR value for MR magnitude image is assumed.

   iv. Gaussian white noise is added to S_1 with standard deviation $sd = \frac{A}{\mathrm{SNR}}$ where A is the mean of S_1 magnitude image. Another Gaussian white noise with the same standard deviation is added to S_2.

   v. Using noisy S_1 and S_2 magnitude images, noisy H^+ magnitude is obtained using the double angle B_1 mapping formula:

$$\left|H^+\right| = \frac{\cos^{-1}(S_2/2S_1)}{k}$$

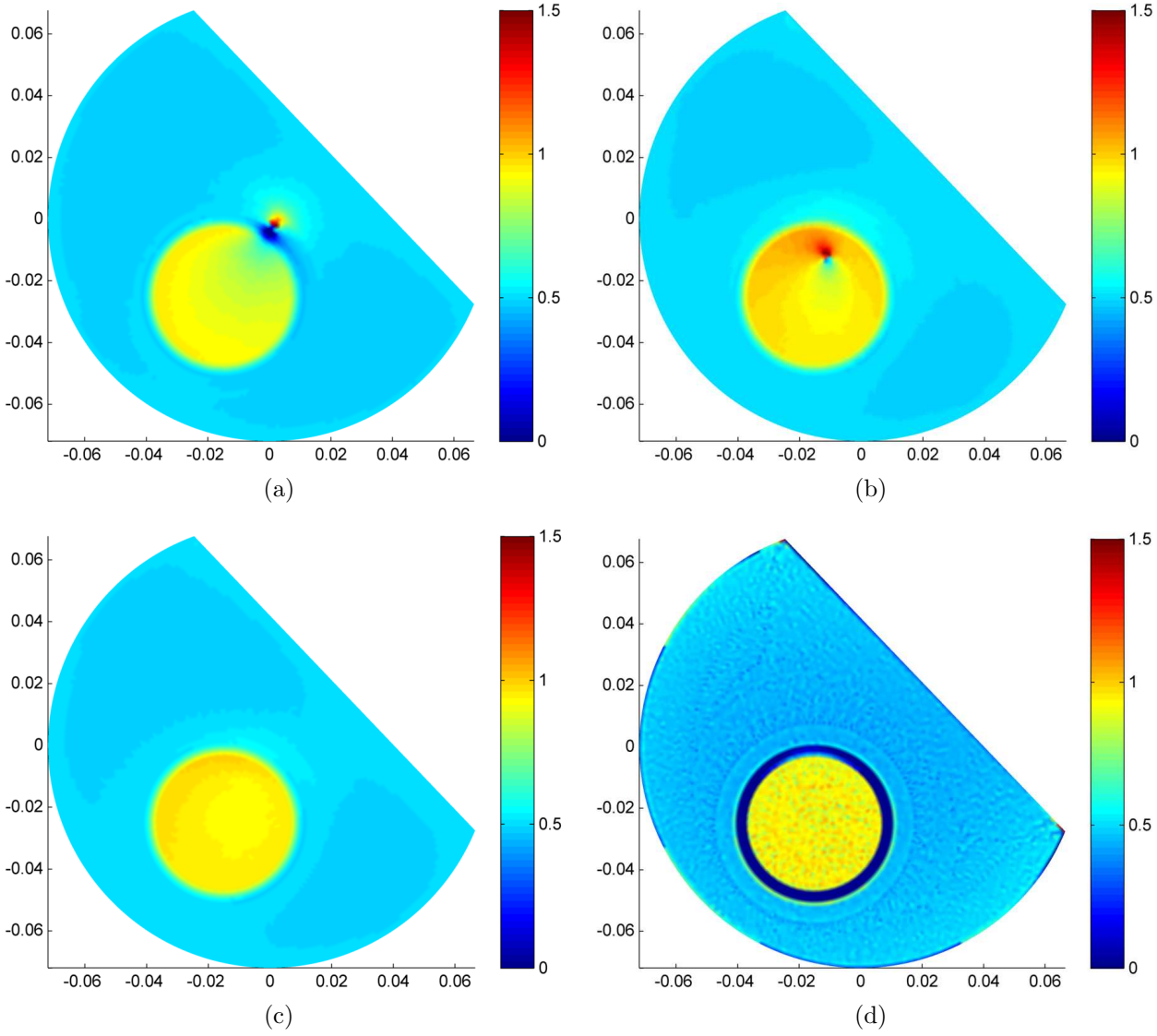

Figure 4.6: Conductivity σ (S/m) reconstruction results for the second simulation phantom: cr-MREPT method is used for (a) only the first excitation and (b) for only the second excitation. (c) double-excitation cr-MREPT method is used, (d) Wen's method is used. The spot-like artifacts observed in (a) and (b) at different locations, are eliminated when double-excitation cr-MREPT method is used as shown in (c).

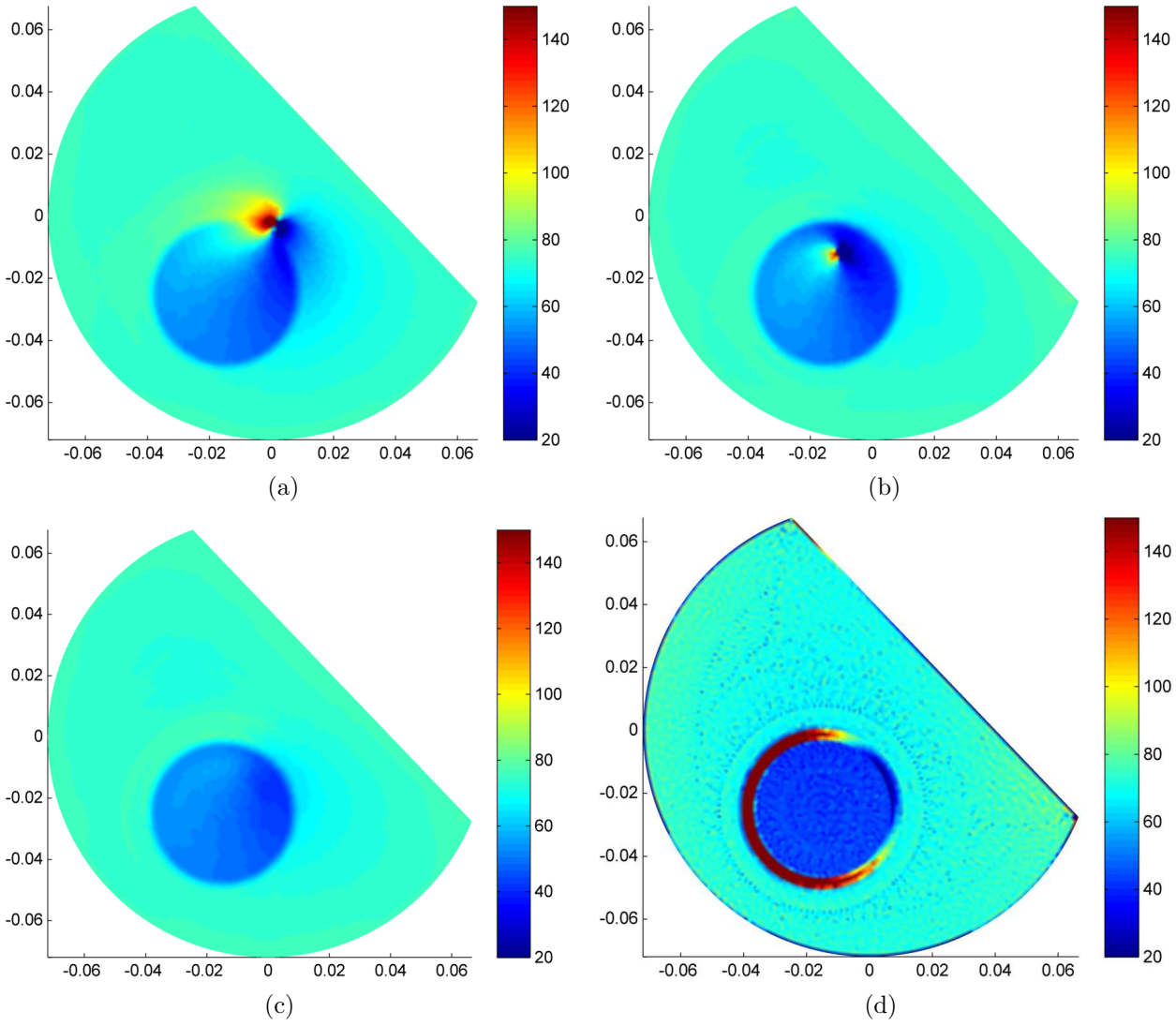

Figure 4.7: Relative dielectric permittivity ε_r reconstruction results for the second simulation phantom: cr-MREPT method is used for (a) only the first excitation and (b) for only the second excitation. (c) double-excitation cr-MREPT method is used, (d) Wen's method is used. The spot-like artifacts observed in (a) and (b) at different locations, are also eliminated when double-excitation cr-MREPT method is used as shown in (c).

b) Obtaining noisy H^+ phase

The noise in MRI phase images is assumed to have zero-mean Gaussian distribution with standard deviation $sd_\Phi = \sqrt{2}/\text{SNR}$ where SNR is the signal-to-noise ratio of the MRI magnitude image [50]. Since H^+ phase is assumed to be half of the MRI spin-echo phase, the noise in H^+ phase image becomes $sd_{\Phi_{H^+}} = 1/(\sqrt{2}\ \text{SNR})$.

c) Obtaining noisy complex H^+

Noisy complex H^+ is obtained from the noisy H^+ magnitude and phase, using Euler's formula.

In the simulations, SNR values of 50, 100, and 150 are used. These SNR values are reasonable for regular MRI scanning. In fact, the SNRs of the MRI magnitude images obtained experimentally throughout this study using this phantom were estimated to be in the range of 50-100.

Errors made in the reconstructed conductivity and permittivity at the slice of interest are calculated using the relative L^2-error formulae:

$$\begin{aligned} \mathrm{E}_{L^2}(\sigma) &= 100\left[\frac{\sum_{j=1}^{N_p}\left(\sigma_j^a-\sigma_j\right)^2}{\sum_{j=1}^{N_p}\left(\sigma_j^a\right)^2}\right]^{1/2} \\ \mathrm{E}_{L^2}(\varepsilon) &= 100\left[\frac{\sum_{j=1}^{N_p}\left(\varepsilon_j^a-\varepsilon_j\right)^2}{\sum_{j=1}^{N_p}\left(\varepsilon_j^a\right)^2}\right]^{1/2} \end{aligned} \tag{4.1}$$

where σ_j^a (ε_j^a) and σ_j (ε_j) are the actual and reconstructed conductivity (permittivity) distributions at the jth node, respectively.

A low pass filter with Gaussian kernel (in the spatial domain) with standard deviation 0.0032 m was applied to the noisy simulated H^+ complex images. The filter was applied using non-linear diffusion based denoising technique [51]. Using the filtered H^+ complex image for different SNR values, the σ and ε are reconstructed and results are given in Figure 4.8 and 4.9.

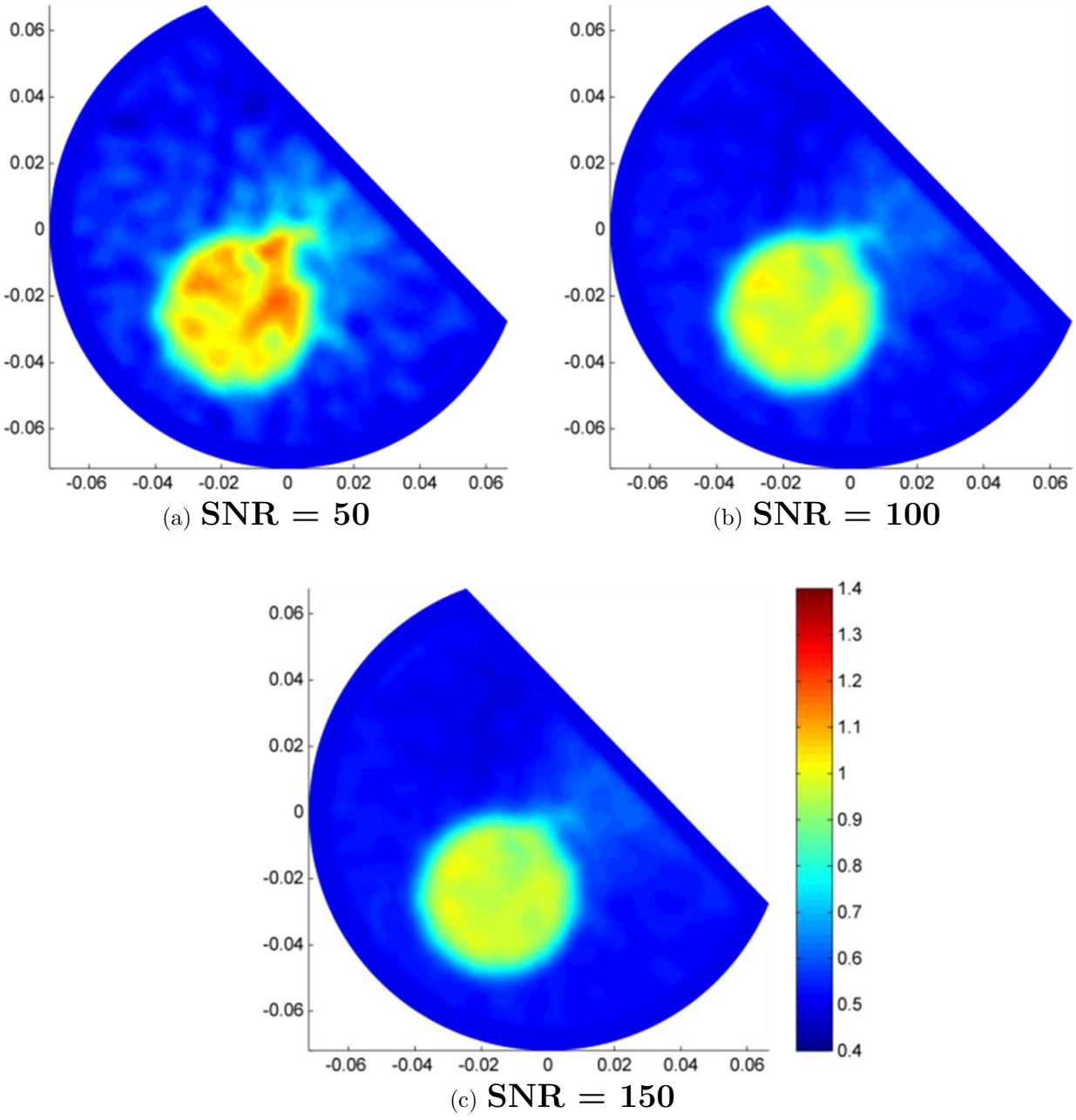

(a) **SNR = 50** (b) **SNR = 100**

(c) **SNR = 150**

Figure 4.8: Double excitation cr-MREPT conductivity σ (S/m) reconstruction results for the second simulation phantom when noise corresponding to SNRs of 50, 100, or 150 is added to each H^+ data obtained for the two excitations.

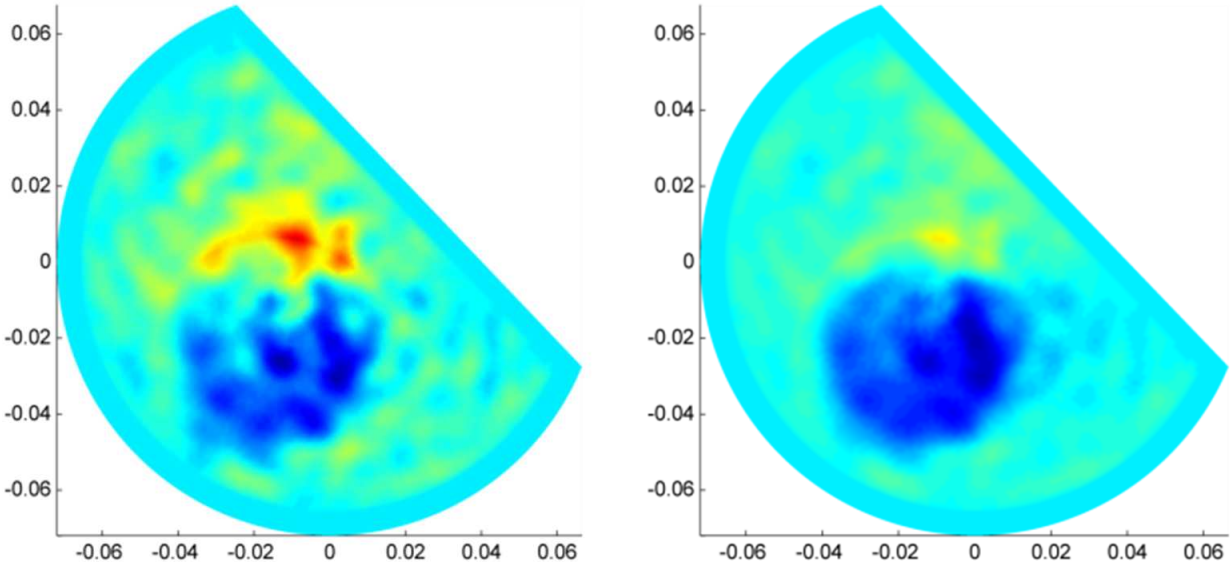

(a) **SNR = 50** (b) **SNR = 100**

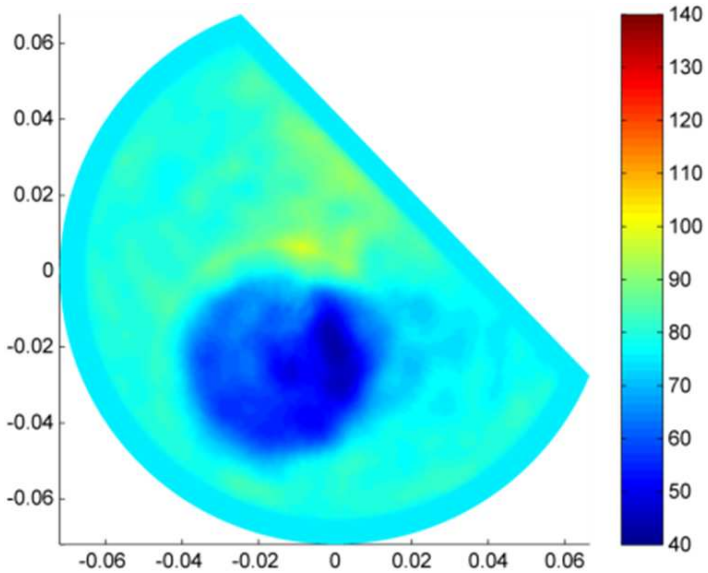

(c) **SNR = 150**

Figure 4.9: Double excitation cr-MREPT relative dielectric permittivity ε_r reconstruction results for the second simulation phantom when noise corresponding to SNRs of 50, 100, or 150 is added to each H^+ data obtained for the two excitations.

As observed in Figure 4.8 and 4.9, the double-excitation cr-MREPT method is robust against noisy H^+ data and it does not generate an artifact in the reconstructed σ and ε distributions in the LCF regions.

For the infinite SNR case (no noise is added), the relative L^2 errors for σ and ε are 8.7% and 9.1% respectively. A significant portion of these errors are due to the low pass filter mentioned above. If the low-pass filter is not used, then for the noiseless case the corresponding relative L^2 errors are 3.7% and 3.9%. The filter tapers the variations of $\nabla^2 H^+$ in the transition regions and consequently blunts the variations of σ and ε across the internal boundaries and thus relative L^2 errors increase. Table 4.1 presents the relative L^2 errors for different SNRs. It may be concluded from these results that for the SNR range of 50-150 acceptable relative L^2 errors are obtained.

Table 4.1: L^2 errors in σ and ε reconstructed using double-excitation cr-MREPT method when noise corresponding to different SNR values added to H^+.

		Relative L^2 error (%)	
SNR	Filter applied	$\mathrm{E}_{L^2}(\sigma)$	$\mathrm{E}_{L^2}(\varepsilon)$
∞	no	3.7	3.9
∞	yes	8.7	9.1
150	yes	9.3	10.0
100	yes	9.8	11.2
50	yes	15.0	18.7

4.2 Experimental Results

Experiments are first conducted using the first experimental phantom. Figure 4.10 shows the measured H^+ magnitude and phase, modulus of $\nabla^2 H^+$, and the modulus of the convective field. They are in good agreement and have similar trends with the simulated data shown in Figure 4.1.

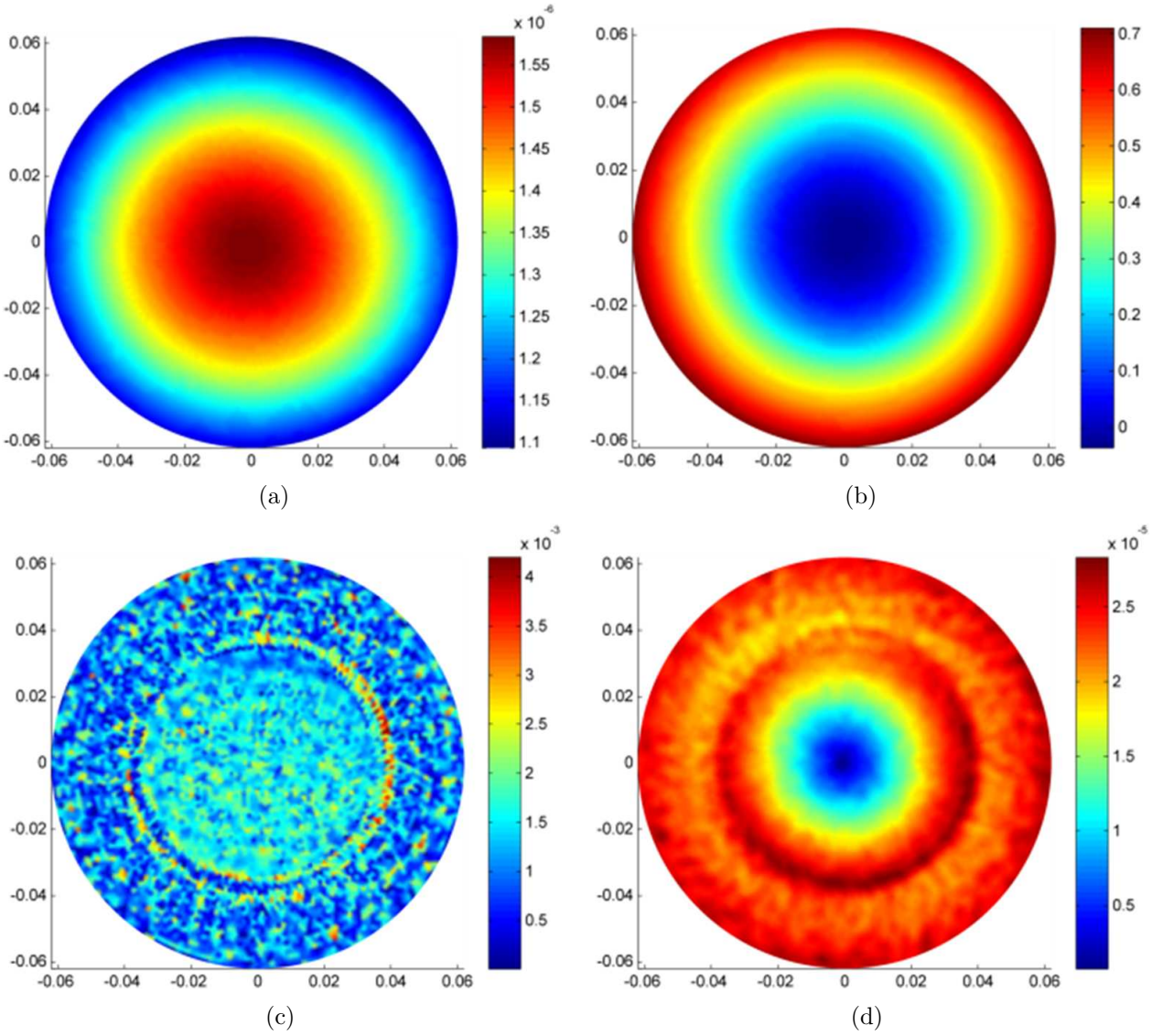

Figure 4.10: Experimental results for the central axial slice of the first experimental phantom, (a) magnitude of B_1^+ (T), (b) phase of B_1^+ (rads), (c) modulus of $\nabla^2 B_1^+$ (T/m^2), (d) modulus of the convective field (T/m).

The same low pass filter, which is used for noisy simulated data as mentioned above, is applied also to the measured H^+ as the first step. Using the filtered H^+, Voigt's method, which is described in Section 1.2, is applied and the reconstructed conductivity distribution is obtained as shown in Figure 4.11(a). In this method, for volume integral and surface integral covering this volume, 4x4x4 voxels or equivalently 5x5x5 samples are selected. Moreover, using the calculated $\nabla^2 H^+$ and convective field, reconstructed conductivity distribution is obtained by applying cr-MREPT methods, and is shown in Figure 4.11(b). Similarly, the result of Voigt's method has severe errors in the transition regions. On the other hand, cr-MREPT is very successful in reconstructing the boundary transitions. However, the result of cr-MREPT method has a spot-like artifact in the LCF region.

When the constrained cr-MREPT method, which is explained in Section 4.1.1, is applied, the reconstructed conductivity shown in Figure 4.11(c) is obtained and it does not have a spot-like artifact. In this method, a circular region with radius of 0.007 m which encloses the spot-like artifact region is first selected. In this region, the averages of the electrical properties found using Wen's method are calculated. These average values are used for this region as a constraint (a-priori knowledge) in the constrained cr-MREPT method. The average conductivity values for the reconstructed distribution shown in Figure 4.11(c) are 0.93 S/m for the inner object and 0.43 S/m for the background. These values are consistent with the estimated values given in Section 3.3.1. When applying the cr-MREPT method, the average conductivity and permittivity values obtained by the Wen's method at the outer boundary are used for assigning the Dirichlet boundary condition required in solving Equation (2.9).

Experiments are then performed using the second experimental phantom. Figure 4.12(a) and (b) show the moduli of the convective fields with and without segment E. As shown in Figure 4.12, these convective fields have different LCF regions that do not coincide with each other. Using the calculated $\nabla^2 H^+$ data of the two cases together, double excitation cr-MREPT method is applied and the reconstructed conductivity distribution is obtained, as shown in Figure 4.12(c). Outer boundary conditions are again taken from the results of the Wen's method.

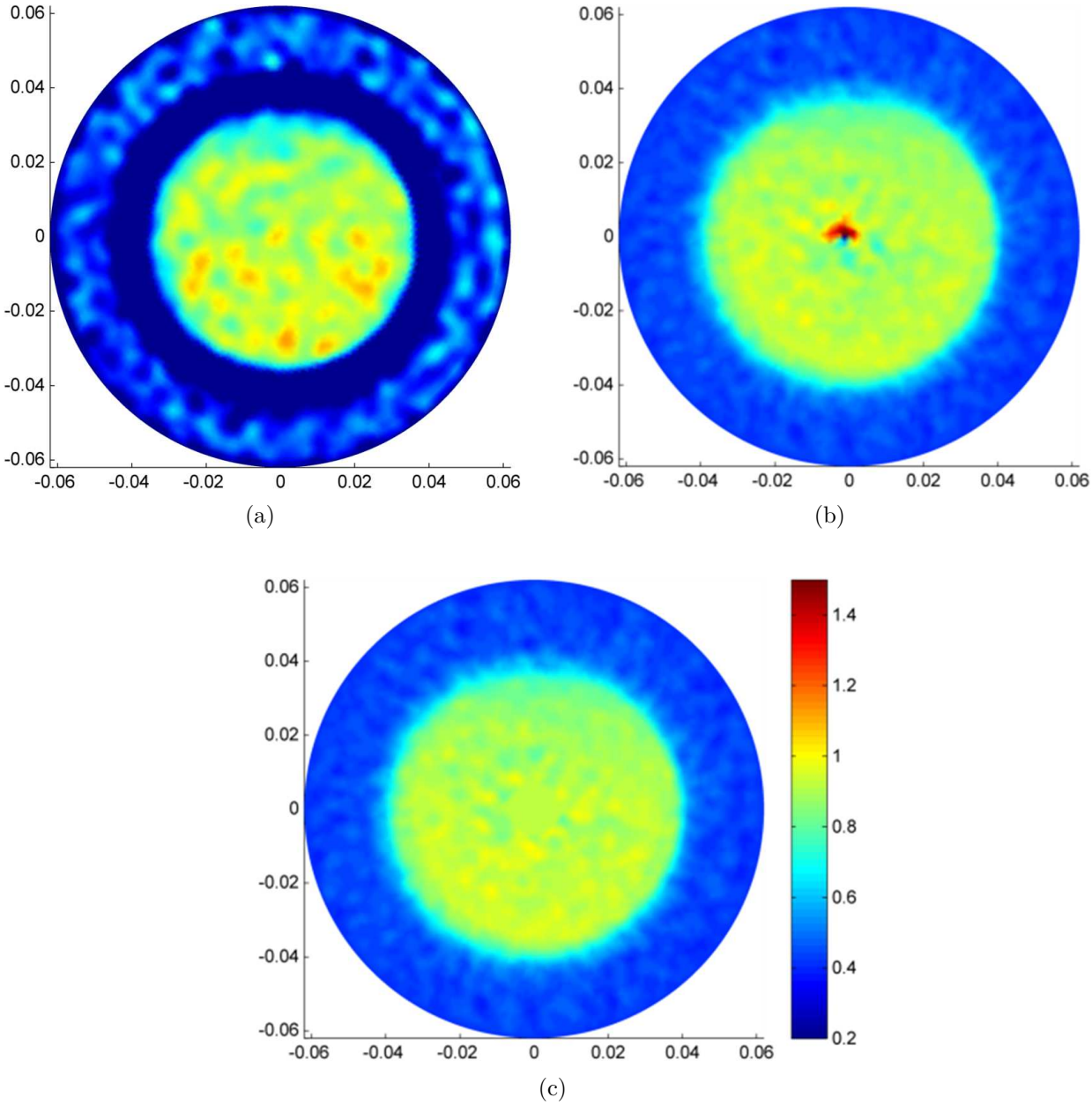

Figure 4.11: Reconstructed conductivity σ (S/m) distributions for the axial slice of the first experimental phantom: (a) Voigt's method, (b) cr-MREPT method, (c) constrained cr-MREPT method.

As expected, the reconstructed conductivity distribution does not have spot-like artifacts, and the boundary transitions are well constructed. The average reconstructed conductivity values are 0.99 S/m for the inner object and 0.45 S/m for the background, again similar to the estimated values.

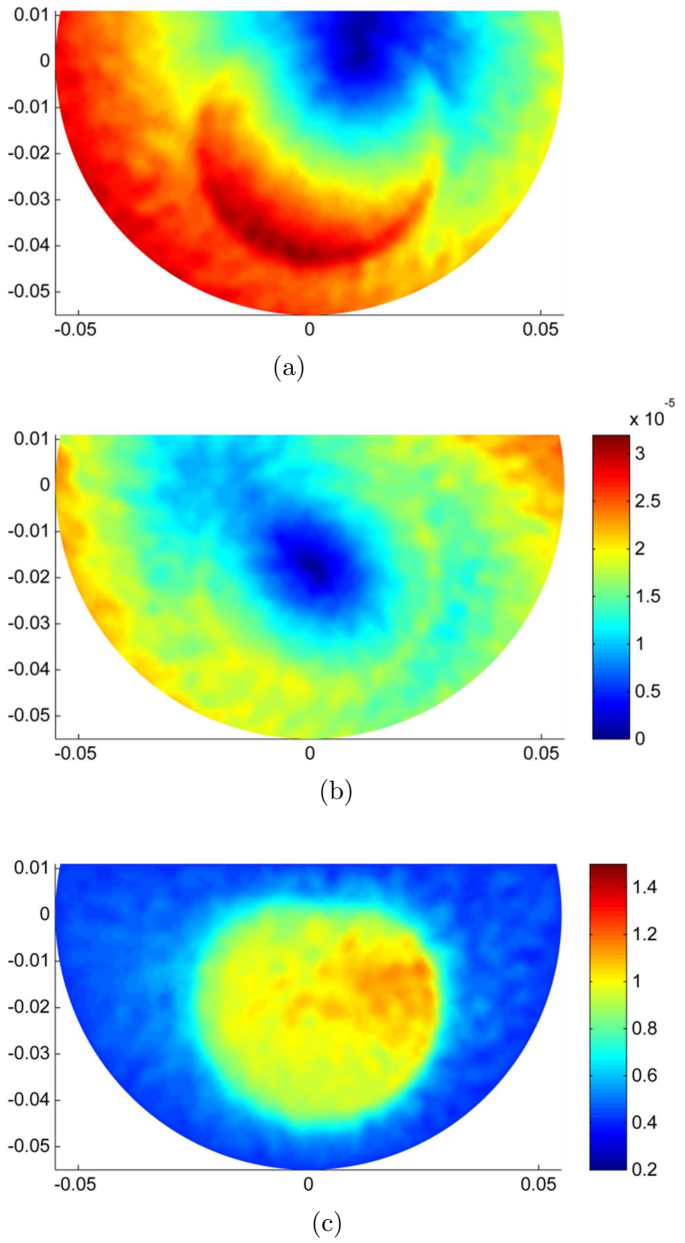

Figure 4.12: For the axial slice of the second experimental phantom, (a) modulus of the convective field (T/m) for the first excitation, (b) modulus of the convective field (T/m) for the second excitation, (c) reconstructed conductivity σ (S/m) distribution using double-excitation cr-MREPT method. Convective fields shown in (a) and (b) have different LCF regions. Note that these images which correspond to the second experimental phantom are presented in a horizontal fashion in contrast to the images previously given in a rotated fashion for the second simulation phantom.

Chapter 5

Convection-Reaction Equation based Magnetic Resonance Electrical Properties Tomography (cr-MREPT) using Finite Element Method (FEM)

In cr-MREPT method, the convection-reaction equation (i.e. Equation (2.9)) can be also solved by different methods. In previous results, a triangular mesh based finite difference method is used. In this chapter, Finite Element Method (FEM) is used to solve the convection-reaction equation.

5.1 Method

In this method, it is assumed that H^+ is measured in Cartesian coordinate system. Then, its first derivatives and the Laplacian of H^+ are calculated using finite difference approximations of derivatives and Laplacian of H^+ is calculated using 3 axial slices in simulations and experiments. The coefficients of the Equation

(2.9) are also calculated in Cartesian coordinates. A mesh is generated by using a FEM software package (we use COMSOL Multiphysics) and the calculated coefficients of the Equation (2.9) are linearly interpolated to the mesh points. Equation (2.9) is then solved using finite element method (FEM). Similarly, for boundary condition Dirichlet boundary condition is also used, i.e., conductivity and dielectric permittivity are specified at the boundary. In this thesis, we used a commercial FEM software tools (COMSOL Multiphysics) to solve the Equation (2.9).

In simulation studies, H^+ is calculated at mesh nodes. Therefore, H^+ in Cartesian coordinates is calculated using linear interpolation. In experimental studies, MR images are already in Cartesian coordinates and the measured H^+ can be found in Cartesian coordinates.

5.2 Simulations

Simulated magnetic field data is generated using COMSOL Multiphysics (COMSOL AB, Sweden) for the phantom shown in Figure 5.1(a). In this phantom two eccentric cylindrical objects with different electrical properties (σ and ε) are placed in a quadrature birdcage coil model. Radius of inner and outer cylindrical objects are 2 cm and 5 cm, respectively and their heights are 10 cm. The cross-sectional conductivity and dielectric permittivity distributions are shown in Figure 5.1(b).

Using simulated H^+ map and FEM method, the solution of Equation (2.9) gives the conductivity and dielectric permittivity reconstructions shown in Figure 5.2(a) and (b). In these figures, a spot-like artifact is observed in Low Convection Field (LCF) region. To eliminate the spot-like artifact, constrained cr-MREPT method is used. The resultant reconstructed conductivity and dielectric permittivity distributions, shown in Figure 5.2(c) and (d), do not have spot-like artifacts.

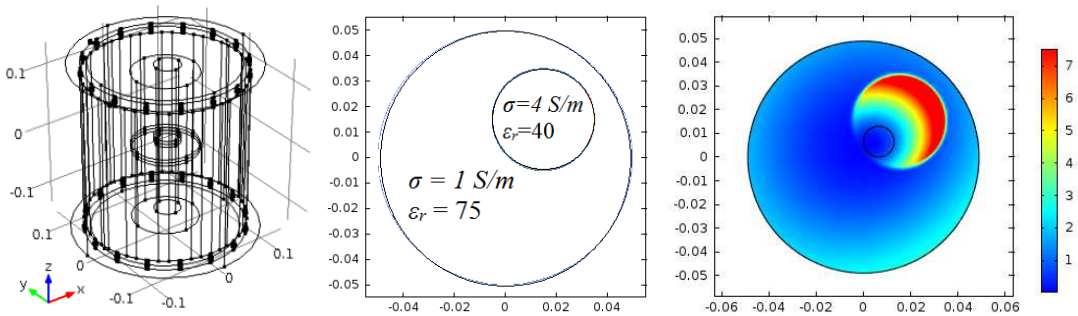

(a) (b) (c)

Figure 5.1: (a) Simulation phantom, (b) simulated actual conductivity and dielectric permittivity, (c) modulus of convective field, unit is arbitrary (black circle shows LCF region).

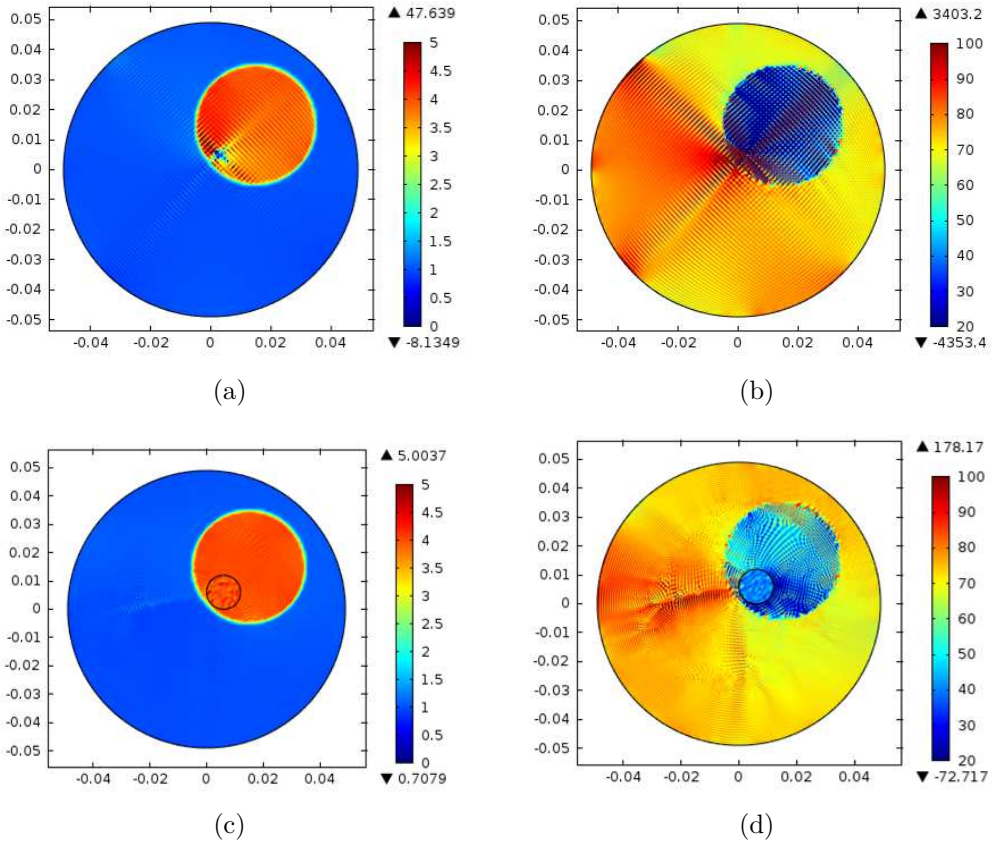

(a) (b) (c) (d)

Figure 5.2: Simulation results of cr-MREPT using FEM: (a) reconstructed conductivity, (b) reconstructed dielectric permittivity, (c) reconstructed conductivity using the constrained cr-MREPT method, (d) reconstructed dielectric permittivity using the constrained cr-MREPT method.

5.3 Experiments

For experimental studies, a rectangular phantom (filled with solution of 1 gr/l $CuSO_4$, 12 gr/l NaCl) which contains a cylindrical bottle (filled with solution of 1 gr/l $CuSO_4$, 2.3 gr/l NaCl) is constructed. The dimensions of the rectangular phantom are 22.5x34x11 cm, the diameter of inner cylindrical object is 7 cm and its height is 15 cm. The conductivity values of the background and inner object are calculated as 2.0 and 0.4 S/m and their relative dielectric permittivity values are calculated as 74.4 and 77.6, respectively [47]. The experiments were performed on a 3T MR scanner (Siemens, Erlangen, Germany) using quadrature transmit/receive coil. H^+ amplitude map is also acquired using double angle method (flip angle = 60deg and 120deg, TR=2000 ms, GRE, 1.6x1.6x5 mm, 3 axial slices). Similarly, H^+ phase map is also approximated as half of the transceive phase for quadrature birdcage coil and transceive phase is acquired by SE experiment (1.6x1.6x5 mm, SE, TR=2000, 3 axial slices). A Gaussian filter with kernel size 5 and standard deviation 1 is applied to the measured complex H^+ maps.

Experiments are conducted using this experimental phantom. Figure 5.3 shows the spin-echo magnitude image, measured B_1^+ magnitude and phase images after the filter is applied.

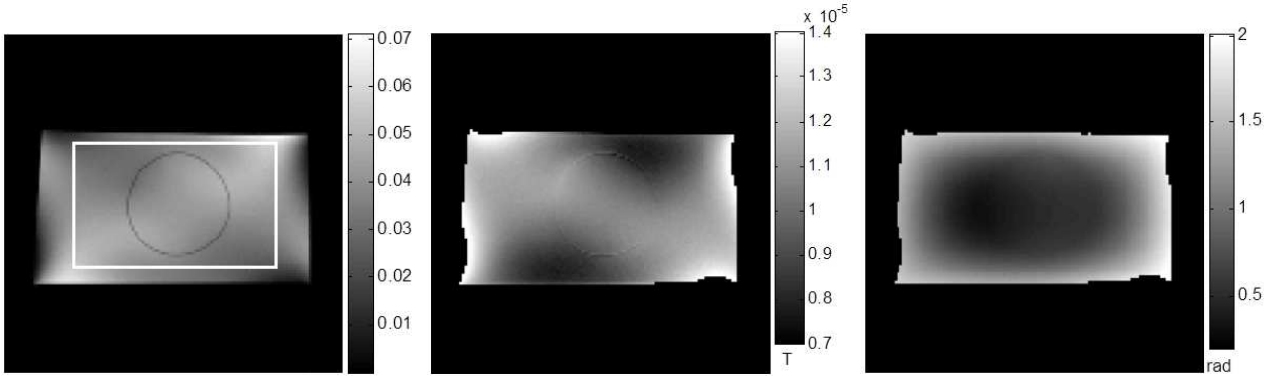

(a) (b) (c)

Figure 5.3: (a) Spin echo magnitude (white rectangle shows the region of interest), (b) B_1^+ magnitude, (c) B_1^+ phase image

Using the measured B_1^+ magnitude and phase, H^+, derivatives and Laplacian of the H^+ are calculated at Cartesian coordinates by applying finite difference approximations of derivatives. Then, the reconstructed conductivity distribution shown in Figure 5.4(a) is obtained by solving Equation (2.9) using FEM method. Similar to simulation results, a spot-like artifact is observed in LCF region. To eliminate this artifact, the constrained cr-MREPT method is used. When this method is applied, the reconstructed conductivity shown in Figure 5.4(b) is obtained and it does not have a spot-like artifact. When Wen's method is applied, the reconstructed conductivity distribution shown in Figure 5.4(c) is obtained. Similar to the previous experimental results, the reconstruction results of Wen's method has severe errors on the internal boundaries but cr-MREPT methods are very successful in reconstructing the boundary regions.

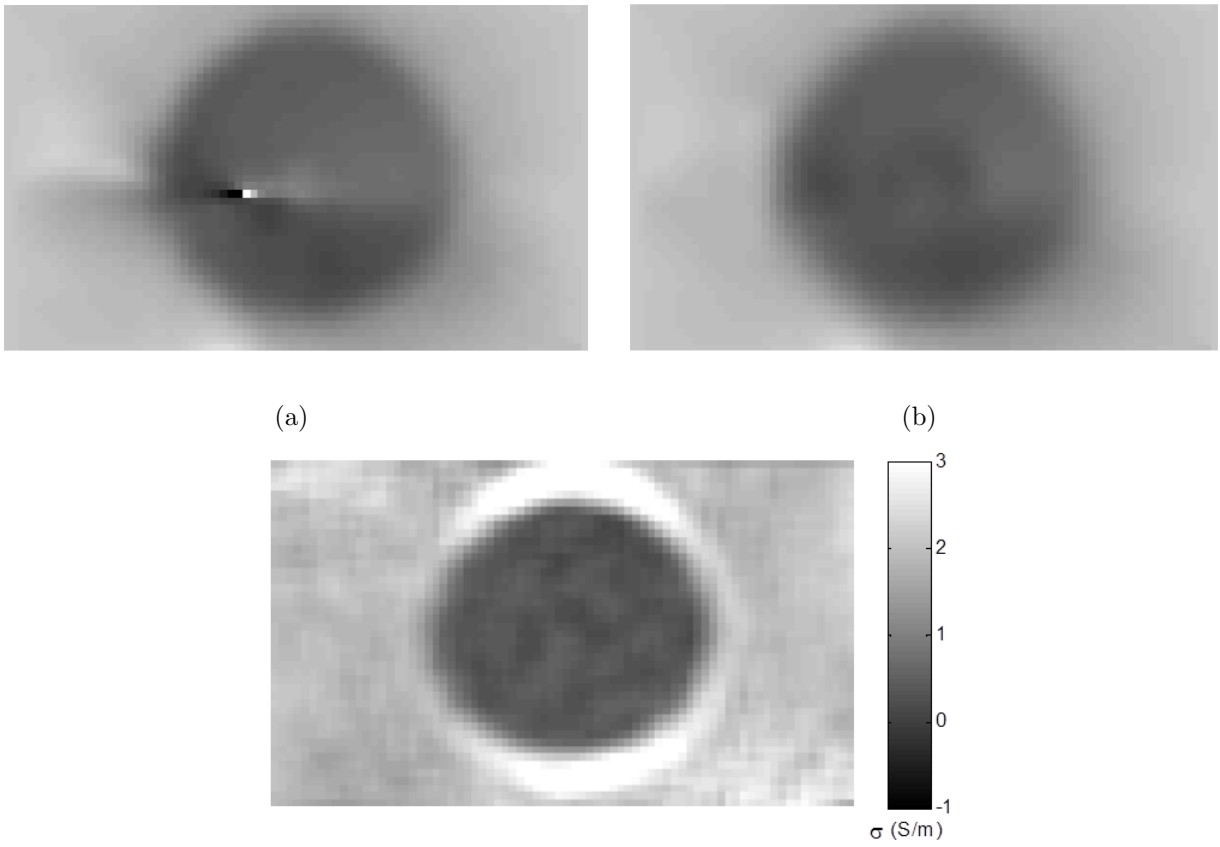

Figure 5.4: Experiment results of cr-MREPT using FEM, reconstructed conductivity σ (S/m) distributions for the axial slice: (a) cr-MREPT method, (b) constrained cr-MREPT method, (c) Wen's method.

Chapter 6

Discussion and Conclusion

Magnetic Resonance Electrical Properties Tomography (MREPT) is developed to reconstruct both the electrical conductivity and the dielectric permittivity of tissues, at the Larmor frequency of the MRI system, in order to provide information for diagnostic purposes, and also for the calculation of the spatial distribution of patient-specific SAR. Although MREPT and MREIT reconstruct high spatial resolution electrical property images at completely different frequencies, nevertheless MREPT has a significant advantage over MREIT because it does not require electrode mounting on the body surface. Furthermore MREPT uses standard MR sequences and does not have a safety burden on the patient. Additionally, it does not have a restriction like the limitation on the maximum amount of applied current in MREIT.

For MREPT, previously developed practical algorithms reconstruct electrical properties in regions where σ and ε values are almost constant [25][26][28]. In this thesis, we have proposed a novel algorithm named convection-reaction equation based MREPT (cr-MREPT) which reconstructs σ and ε also in transition regions where σ and ε vary. However, spot-like artifacts are observed in the regions where the convection field is low. To eliminate these artifacts, we have proposed two different correction techniques named as "constrained cr-MREPT" and "double-excitation cr-MREPT". We have validated these MREPT algorithms using both simulated and experimental data. The "constrained cr-MREPT" method has the

limitation that it can not be applied in the LCF regions which have varying σ and ε. For the "double-excitation cr-MREPT" method, we have removed part of the object (region E of the phantom shown in Figure 3.4(b)) in order to generate a second B_1^+ distribution. Obviously, this procedure can not be applied to human subjects. Therefore, we propose that an additional object is attached to one side of the body in order to distort the internal B_1^+ field. The determination of the exact shape, position, material, and electrical properties of such a contacting object is the subject of further studies.

In this thesis, the derived convection-reaction equation of MREPT is solved using a triangular mesh based finite difference method. We have used the mesh generation facility of COMSOL Multiphysics in order to obtain a triangular mesh. The solution of the equation itself can also be done by FEM or other numerical methods. In previously published work, a convection equation based formulation is developed for MREIT and the numerical solution was based on FEM [52]. Some specific problems which arise when a commercial FEM package is used for the solution are discussed in [52]. We also applied a FEM based solution method for constrained cr-MREPT [53]. Extension of FEM to the double excitation cr-MREPT and also use of regularization and stabilization methods will be considered in future studies.

The cr-MREPT algorithm requires magnitude and phase of B_1^+ measurements to reconstruct σ and ε distributions. Many B_1^+ mapping techniques have been proposed to measure magnitude of the field [30][32][40]-[42] whereas there is no exact and general method to measure B_1^+ phase. B_1^+ phase mapping has been studied by several groups and it has been argued that the B_1^+ phase is equal to half the transceive phase in many situations, e.g., circular symmetry [25][26][28]. In general, development of more accurate and robust B_1^+ complex image mapping techniques will help to improve the efficiency and accuracy of all MREPT algorithms.

In the cr-MREPT algorithm, the z-component of the magnetic field intensity H_z is neglected. In the case of a RF birdcage coil, H_z in the central imaging slice is generated mainly by the end-rings of the RF birdcage coil. However, the

magnitude of this H_z is small enough not to influence our reconstructed images. When TEM coils are used, better reconstruction results with higher accuracy can be obtained [27]. On the other hand, H_z can be estimated from a full model including the birdcage coil and the patient, and/or it can be found by iterative computation [26][31].

Noise tolerance of our algorithm is also investigated for different noise levels. Since the Laplacian operation, used in finding $\nabla^2 H^+$, amplifies the noise, the cr-MREPT method is relatively sensitive to noise. A low pass filter with Gaussian kernel with standard deviation 0.0032 m is applied when processing both the noisy simulated data and the experimental data. This filtering causes the transition regions, where electrical properties vary, to appear wider in the reconstructed images. Therefore, in determining the standard deviation of the Gaussian kernel, this tradeoff between having less noisy reconstructions and having higher spatial resolution must be taken into consideration.

Bibliography

[1] C. Gabriel, S. Gabriel, and E. Courhout, "The dielectric properties of biological tissues: I. literature survey," *Phys. Med. Biol.*, vol. 41, pp. 2231–2249, Nov. 1996.

[2] E. C. Fear, X. Li, S. C. Hagness, and M. A. Stuchly, "Confocal microwave imaging for the breast cancer detection: Localization of tumors in three dimensions," *IEEE Trans. Biomed. Eng.*, vol. 49, pp. 812–822, Aug. 2002.

[3] W. T. Joines, Y. Zhang, C. Li, and R. L. Jirtle, "The measured electrical properties of normal and malignant human tissues from 50 to 900 mhz," *Med. Phys.*, vol. 21, pp. 547–550, Apr. 1994.

[4] A. J. Surowiec, S. S. Stuchly, J. B. Barr, and A. Swarup, "Dielectric properties of breast carcinoma and the surrounding tissues," *IEEE Trans. Biomed. Eng.*, vol. 35, pp. 257–263, Apr. 1988.

[5] S. Gabriel, R. W. Lau, and C. Gabriel, "The dielectric properties of biological tissues: Ii. measurements in the frequency range 10 hz to 20 ghz," *Phys. Med. Biol.*, vol. 41, p. 2251?2269, Nov. 1996.

[6] L. T. Muftuler, M. Hamamura, O. Birgul, and O. Nalcioglu, "Resolution and contrast in magnetic resonance electrical impedance tomography (mreit) and its application to cancer imaging," *Techn. Canc. Res. Treat.*, vol. 3, pp. 599–609, Dec. 2004.

[7] V. Cherepenin, A. Karpov, A. Korjenevsky, V. Kornienko, A. Mazaletskaya, D. Mazourov, and D. Meister, "A 3d electrical impedance tomography (eit)

system for breast cancer detection," *Physiol. Meas.*, vol. 22, pp. 9–18, Feb. 2001.

[8] L. Liu, W. Dong, X. Ji, L. Chen, L. Chen, W. He, and J. Jia, "A new method of noninvasive brain-edema monitoring in stroke: cerebral electrical impedance measurement.," *Neurological Research*, vol. 28, no. 1, pp. 31 – 37, 2006.

[9] A. C. Zelinski, L. M. Angelone, V. K. Goyal, G. Bonmassar, E. Adalsteinsson, and L. L. Wald, "Specific absorption rate studies of the parallel transmission of inner-volume excitations at 7T," *Journal of Magnetic Resonance Imaging*, vol. 28, no. 4, pp. 1005–1018, 2008.

[10] A. McEwan, G. Cusick, and D. S. Holder, "A review of errors in multi-frequency eit instrumentation," *Physiol. Meas.*, vol. 28, pp. 197–215, 2007.

[11] D. C. Barber and B. H. Brown, "Applied potential tomography," *Journal of Physics E: Scientific Instruments*, vol. 17, pp. 723–733, 1984.

[12] L. F. Fuks, M. Cheney, D. Isaacson, D. G. Gisser, and J. C. Newell, "Detection and imaging of electric conductivity and permittivity at low frequency," *IEEE Trans. Biomed. Eng.*, vol. 38, p. 1106?1110, Nov. 1991.

[13] P. M. Edic, G. J. Saulnier, J. C. Newell, and D. Isaacson, "A real-time electrical impedance tomograph," *IEEE Trans. Biomed. Eng.*, vol. 42, pp. 849–859, Sep. 1995.

[14] N. G. Gencer, Y. Z. Ider, and S. J. Williamson, "Electrical impedance tomography: Induced-current imaging achieved with a multiple coil system," *IEEE Trans. Biomed. Eng.*, vol. 43, pp. 139–149, Feb. 1996.

[15] H. Griffiths, "Magnetic induction tomography," *Meas. Sci. Technol.*, vol. 12, pp. 1126–1131, Aug. 2001.

[16] Y. Z. Ider and S. Onart, "Algebraic reconstruction for 3d magnetic resonance-electrical impedance tomography (mreit) using one component of magnetic flux density," *Physiol. Meas.*, vol. 25, pp. 281–294, Feb. 2004.

[17] O. Birgul and Y. Z. Ider, "Use of the magnetic field generated by the internal distribution of injected currents for electrical impedance tomography," in *Proc. 9th Int. Conf. on Bio-Impedance*, (Heidelberg, Germany), 1995.

[18] Y. Z. Ider and O. Birgul, "Use of the magnetic field generated by the internal distribution of injected currents for electrical impedance tomography (mreit)," *Elektrik Turk. J. Electr. Comput. Sci.*, vol. 6, pp. 215–225, 1998.

[19] J. K. Seo, O. Kwon, and E. J. Woo, "Magnetic resonance electrical impedance tomography (mreit); conductivity and current density imaging," *J. Phys. Conf. Ser.*, vol. 12, pp. 140–155, 2005.

[20] E. J. Woo and J. K. Seo, "Magnetic resonance electrical impedance tomography (mreit) for high-resolution conductivity imaging," *Physiol. Meas.*, vol. 29, pp. R1–R26, 2008.

[21] J. K. Seo, J. R. Yoon, E. J. Woo, and O. Kwon, "Reconstruction of conductivity and current density images using only one component of magnetic field measurements," *IEEE Trans. Med. Imaging*, vol. 97, pp. 1121–1124, 2003.

[22] H. S. Nam, C. Park, and O. I. Kwon, "Non-iterative conductivity reconstruction algorithm using projected currrent density in mreit," *Phys. Med. Biol.*, vol. 53, pp. 6947–6961, 2008.

[23] G. C. Scott, M. L. G. Joy, R. L. Armstrong, and R. M. Henkelman, "Measurement of nonuniform current density by magnetic resonance," *IEEE Trans. Med. Img.*, vol. 10, p. 362?374, Sep. 1991.

[24] L. T. Muftuler and Y. Z. Ider, "Measurement of ac magnetic field distribution using magnetic resonance imaging," *IEEE Trans. Med. Imaging*, vol. 16, pp. 617–622, 1997.

[25] H. Wen, "Noninvasive quantitative mapping of conductivity and dielectric distributions using rf wave propagation effects in high-field mri," *in Proc. SPIE*, vol. 471-477, p. 5030, 2003.

[26] U. Katscher, T. Voigt, C. Findeklee, P. Vernickel, K. Nehrke, and O. Dossel, "Determination of electrical conductivity and local sar via b1 mapping," *IEEE Trans. Med. Imag.*, vol. 28, pp. 1365–1374, Sep. 2009.

[27] X. Zhang, S. Zhu, and B. He, "Imaging electric properties of biological tissues by rf field mapping in mri," *IEEE Trans. Med. Imag.*, vol. 29, pp. 474–481, Feb. 2010.

[28] A. L. van Lier, D. O. Brunner, K. P. Pruessmann, D. W. Klomp, P. R. Luijten, J. J. Lagendijk, and C. A. van den Berg, "B1+ phase mapping at 7 t and its application for in vivo electrical conductivity mapping.," *Magnetic Resonance in Medicine*, pp. 1–10, March 2011.

[29] E. M. Haacke, L. S. Petropoulos, E. W. Nilges, and D. H. Wu, "Extraction of conductivity and permittivity using magnetic resonance imaging," *Physics in Medicine and Biology*, vol. 36, no. 6, p. 723, 1991.

[30] S. Akoka, F. Franconi, F. Seguin, and A. le Pape, "Radiofrequency map of an nmr coil by imaging," *Magn. Reson. Imag.*, vol. 11, pp. 437–441, 1993.

[31] U. Katscher, T. Dorniok, C. Findeklee, P. Vernickel, and K. Nehrke, "In vivo determination of electric conductivity and permittivity using a standard mr system," in *IFMBE Proc. H. Scharfetter and R. Merwa*, (Berlin, Germany), pp. 508–511, 2007.

[32] V. L. Yarnykh, "Actual flip-angle imaging in the pulsed steady state: A method for rapid three-dimensional mapping of the transmitted radiofrequency field," *Magn. Reson. Med.*, vol. 57, pp. 192–200, Jan. 2007.

[33] T. Voigt, U. Katscher, and O. Doessel, "Quantitative conductivity and permittivity imaging of the human brain using electric properties tomography," *Magnetic Resonance in Medicine*, vol. 66, no. 2, pp. 456–466, 2011.

[34] J. K. Seo, M.-O. Kim, J. Lee, N. Choi, E. J. Woo, H. J. Kim, O. I. Kwon, and D.-H. Kim, "Error analysis of nonconstant admittivity for mr-based electric property imaging," *Medical Imaging, IEEE Transactions on*, vol. 31, no. 2, pp. 430–437, 2012.

[35] D. K. Sodickson, L. Alon, C. M. Deniz, R. Brown, B. Zhang, G. C. Wiggins, G. Y. Cho, N. B. Eliezer, D. S. Novikov, R. Lattanzi, Q. Duan, L. A. Sodickson, and Y. Zhu, "Local maxwell tomography using transmit-receive coil arrays for contact-free mapping of tissue electrical properties and determination of absolute rf phase," in *Proceedings of the 20th Annual Meeting of ISMRM*, (Melbourne, Australia), 2012.

[36] D. I. Hoult, "The principle of reciprocity in signal strength calculations-a mathematical guide," *Concepts Magn. Reson.*, vol. 12, p. 173?187, 2000.

[37] O. Zienkiewicz, R. Taylor, and J. Zhu, *The Finite Element Method: Its Basis and Fundamentals: Its Basis and Fundamentals*. Elsevier Science, 2005.

[38] J. F. Schenck, "The role of magnetic susceptibility in magnetic resonance imaging: MRI magnetic compatibility of the first and second kinds," *Medical Physics*, vol. 23, pp. 815–850, June 1996.

[39] U. Katscher, D.-H. Kim, and J. K. Seo, "Recent progress and future challenges in mr electric properties tomography," *Computational and Mathematical Methods in Medicine*, vol. 2013, 2013.

[40] R. Stollberger and P. Wach, "Imaging of the active b1 field in vivo," *Magn. Reson. Med.*, vol. 35, pp. 246–251, Feb. 1996.

[41] J. Wang, M. Qiu, Q. X. Yang, M. B. Smith, and R. T. Constable, "Measurement and correction of transmitter and receiver induced nonuniformities in vivo," *Magn. Reson. Med.*, vol. 53, pp. 408–417, Feb. 2005.

[42] L. I. Sacolick, F. Wiesinger, I. Hancu, and M. W. Vogel, "B1 mapping by bloch-siegert shift," *Magn. Reson. Med.*, vol. 63, pp. 1315–1322, May 2010.

[43] F. A. Fernandez and L. Kulas, "A simple finite difference approach using unstructured meshes from fem mesh generators," *15th International Conference on Microwaves Radar and Wireless Communications IEEE*, vol. 2, pp. 585–588, May 2004.

[44] Y. Duan, T. S. Ibrahim, B. S. Peterson, F. Liu, and A. Kanfarlu, "Assessment of a pml boundary condition for simulating an mri radio frequency coil," *International Journal of Antennas and Propagation*, p. 10, 2008.

[45] N. Gurler and Y. Z. Ider, "Fem based design and simulation tool for mri birdcage coils including eigenfrequency analysis," in *COMSOL Proc.*, (Milan, Italy), 2012.

[46] N. Gurler, F. S. Hafalir, O. F. Oran, and Y. Z. Ider, "A new accurate fem based optimization method for birdcage coil design at high field strength," in *Proceedings of the 21th Annual Meeting of ISMRM*, (Utah, USA), 2013.

[47] A. Stogryn, "Equations for calculating the dielectric constant of saline water," *IEEE Trans. Microwave. Theory Tech.*, vol. 19, pp. 733–736, Aug. 1971.

[48] F. Kremer and A. Schönhals, *Broadband Dielectric Spectroscopy.* Springer Verlag, 2003.

[49] W. R. Overall, J. M. Pauly, P. P. Stang, and G. C. Scott, "Ensuring safety of implanted devices under mri using reversed rf polarization," *Magnetic Resonance in Medicine*, vol. 64, no. 3, pp. 823–833, 2010.

[50] G. Scott, M. Joy, R. Armstrong, and R. Henkelman, "Sensitivity of magnetic-resonance current-density imaging," *Journal of Magnetic Resonance*, vol. 97, pp. 235–254, April 1992.

[51] D. Tschumperle and R. Deriche, "Diffusion pdes on vector-valued images," *IEEE Signal Processing Magazine*, vol. 19, pp. 16–25, Sep. 2002.

[52] O. F. Oran and Y. Z. Ider, "Magnetic resonance electrical impedance tomography (mreit) based on the solution of the convection equation using fem with stabilization," *Phys. Med. Biol*, vol. 57, pp. 5113–5140, 2012.

[53] F. S. Hafalir, O. F. Oran, N. Gurler, and Y. Z. Ider, "Magnetic resonance electrical properties tomography (mrept) based on the solution of the convection-reaction equation," in *Proceedings of the 21th Annual Meeting of ISMRM*, (Utah, USA), 2013.